

Abundance and properties of dark radiation from the cosmic microwave background

Murali M. Saravanan,^{a,1} Thejs Brinckmann,^{b,c} Marilena Loverde,^a
Zachary J. Weiner^{a,d}

^aDepartment of Physics, University of Washington, Seattle, WA, USA

^bDipartimento di Fisica e Scienze della Terra, Università degli Studi di Ferrara, Ferrara, Italy

^cIstituto Nazionale di Fisica Nucleare (INFN), Sezione di Ferrara, Ferrara, Italy

^dPerimeter Institute for Theoretical Physics, Waterloo, Ontario, Canada

E-mail: msarav@uw.edu, mloverde@uw.edu, zweiner@perimeterinstitute.ca

Abstract. We study the cosmological signatures of new light relics that are collisionless like standard neutrinos or are strongly interacting. We provide a simple and succinct rephrasing of their physical effects in the cosmic microwave background, as well as the resulting parameter degeneracies with other cosmological parameters, in terms of the total radiation abundance and the fraction thereof that freely streams. In these more general terms, interacting and noninteracting light relics are differentiated by their respective decrease and increase of the free-streaming fraction, and, moreover, the scale-dependent interplay thereof with a common, correlated reduction of the fraction of matter in baryons. We then derive updated constraints on various dark-radiation scenarios with the latest cosmological observations, employing this language to identify the physical origin of the impact of each dataset. The “PR4” reanalyses of *Planck* CMB data prefer a larger primordial helium yield and therefore also slightly more radiation than the 2018 analysis, whose origin we identify in a number of poorly fit polarization measurements. Smaller free-streaming fractions are disfavored by the excess lensing of the CMB measured in lensing reconstruction data from *Planck* and the Atacama Cosmology Telescope. On the other hand, baryon acoustic oscillation measurements from the Dark Energy Spectroscopic Instrument drive marginal detections of new, strongly interacting light relics due to that data’s preference for lower matter fractions. Finally, we forecast measurements from the CMB-S4 experiment.

¹Corresponding author.

Contents

1	Introduction	2
2	Dark radiation and degeneracies in the CMB	2
2.1	Varying radiation density at fixed free-streaming fraction	4
2.1.1	Tilt degeneracy	7
2.1.2	Running of the spectral tilt	9
2.1.3	Degeneracy with the helium fraction	9
2.2	Varying free-streaming fraction at fixed radiation density	10
2.2.1	Shift degeneracy	11
2.3	Free-streaming versus fluidlike radiation	12
2.3.1	Interplay between free-streaming radiation and pressure supported matter	13
2.4	Breaking degeneracies with large scale structure	16
3	Constraints on dark radiation	18
3.1	Impact of recent data on radiation density and composition	20
3.1.1	<i>Planck</i> PR3 versus PR4	20
3.1.2	Role of CMB lensing data	22
3.1.3	Preference for additional radiation with BAO data	24
3.2	Constraints on interacting and noninteracting dark radiation	26
3.3	Forecasts for CMB-S4	27
4	Conclusions	29
A	Constraining power of different multipole ranges	31
B	Supplementary results	32

1 Introduction

Measurements of the cosmic microwave background (CMB) precisely determine cosmological parameters and enable tests of the Λ -cold-dark-matter (Λ CDM) model against other extended cosmologies [1]. In particular, the CMB is a powerful probe of physics beyond the Standard Model (BSM) that feature new light particles. Even light relics that interact too weakly with the Standard Model to be detected in laboratory experiments can still be produced at an appreciable level at the high temperatures of the early Universe, making cosmological probes especially powerful. Neutrinos are one example of such a relic found within the Standard Model (SM) itself. Other examples beyond the SM include axions and axionlike particles, sterile neutrinos, models with nonstandard neutrino interactions, and more general dark sector particles [2–19]. Since the CMB is a precision probe of the Universe at the end of the radiation-dominated epoch, it is sensitive to this “dark” radiation. Even if these light relics have no nongravitational interactions with the SM at times close to recombination, they still leave signatures in the CMB through gravity alone [20, 21].

The light relics predicted in BSM models need not free stream like SM neutrinos do after the weak interactions decouple. In some cases, new particles maintain sufficient self-interaction strength within their own sector that they can be treated as tightly coupled; we refer to this as fluidlike radiation (see, e.g., Refs. [7, 8, 22]). Fortunately, the CMB can distinguish between free-streaming and fluidlike radiation and can therefore shed light on broad classes of BSM models while remaining agnostic to their microphysical details. This potential motivates an ongoing effort to study phenomenological parametrizations of dark radiation sectors with current CMB data [15, 23–29]. Searches for additional light degrees of freedom remain an important science driver for future CMB experiments, such as Simons Observatory [30] and CMB-S4 [31].

A clear theoretical understanding of the differences between the fluidlike and free-streaming radiation is required to maximize the discovery potential for future surveys. Building on prior work, we outline how parameter degeneracies differ between models with extra free-streaming radiation versus extra fluidlike radiation. In Section 2, we put these scenarios on a common, more transparent footing by considering general scenarios parametrized by the total radiation content and its partitioning into free-streaming and fluidlike forms. We detail two partial degeneracy directions deriving from the distinctive physical effects each parameter controls: a “tilt degeneracy” associated with the impact of radiation density on the background cosmology and a “shift degeneracy” arising from the impact of free-streaming perturbations on the photon-baryon plasma. In Section 3 we then provide updated *Planck* constraints on models with new light relics using the latest PR4 dataset [32, 33], CMB lensing data from the Atacama Cosmology Telescope [34, 35] (ACT), and baryon acoustic oscillation (BAO) data from the Dark Energy Spectroscopic Instrument [36–38] (DESI). Throughout, we apply the language developed in Section 2 to explain the physical origin of these results, highlighting cases in which particular datasets have a differing impact on parameter inference for fluidlike and free-streaming light relics. Lastly, we forecast constraints achieved by the current planned configuration for CMB-S4 [31, 39]. We summarize and conclude in Section 4.

2 Dark radiation and degeneracies in the CMB

The energy density in radiation determines the background expansion rate in the early Universe, controlling physical scales like the sound horizon and the diffusion scale [40, 41].

However, the CMB is sensitive not only to the total amount of radiation but also to its properties via the dynamics of spatial perturbations. Perturbations of these additional light relics and their impact on the CMB power spectra are well studied [20, 21, 24]. Broadly speaking, the effects of perturbations are twofold: they impact the amplitude of the CMB power spectrum and shift the angular locations of its extrema. The magnitude of these effects can be calculated analytically by expanding the Boltzmann equations in the fraction of the total radiation density (ρ_r) that freely streams (ρ_{fs}), defined as $f_{\text{fs}} \equiv \rho_{\text{fs}}/\rho_r$. In this section we review the separate impacts of the total density (Section 2.1) and the free-streaming fraction (Section 2.2) on the CMB, remaining agnostic to the actual particle content (aside from the photons). We then apply these results in Section 2.3 to compare and contrast the signatures of new light relics that freely stream like SM neutrinos or are instead fluidlike. Before proceeding, we establish notation.

Following convention, we parametrize the contributions to the radiation density as

$$\rho_r = \rho_\gamma + \rho_\nu + \rho_{\text{BSM}} = \rho_\gamma \left[1 + \frac{7}{8} \left(\frac{4}{11} \right)^{4/3} (N_{\text{fs}} + N_{\text{fld}}) \right], \quad (2.1)$$

where ρ_γ , ρ_ν and ρ_{BSM} are the energy densities in photons, neutrinos and any BSM sectors. We define the total effective number of relativistic species as

$$N_{\text{tot}} \equiv N_{\text{fs}} + N_{\text{fld}} \quad (2.2)$$

where N_{tot} counts the total effective number of degrees of freedom in light relics, N_{fs} those that are free-streaming, and N_{fld} those that are fluidlike. Note that N_{fld} parametrizes the energy density of fluidlike radiation from BSM particles but not from photons, which are effectively fluidlike before recombination due to their interactions with electrons. The above parametrization of the radiation density allows us to write the free-streaming fraction as

$$f_{\text{fs}} \equiv \frac{\rho_{\text{fs}}}{\rho_r} = \frac{7/8 \cdot (4/11)^{4/3} N_{\text{fs}}}{1 + 7/8 \cdot (4/11)^{4/3} N_{\text{tot}}}. \quad (2.3)$$

In the standard Λ CDM model, $f_{\text{fs}} \approx 0.4087$ as the SM predicts $N_{\text{tot}} = N_{\text{fs}} = 3.044$. When allowing for dark radiation in addition to the SM neutrinos' $N_{\text{fs}} = 3.044$, CMB data alone constrain fluidlike radiation to $N_{\text{fld}} < 0.47$ at the 95th percentile but places more stringent constraints on additional free-streaming relics of $\Delta N_{\text{fs}} < 0.37$ (as we derive in Section 3.2). Some current CMB lensing and BAO datasets impact these constraints to a different degree for free-streaming and fluidlike radiation, with some combinations hinting at marginal preferences for the latter (see Section 3.1.3). One of the primary goals of this work is to assess whether these results might indicate the presence of fluidlike light relics or merely reflect discrepancies in parameter inference between different datasets. Moreover, we forecast how future observations will differentiate between free-streaming and fluidlike radiation.

We define ω_b , ω_c , ω_Λ , ω_γ , and ω_ν as the usual present-day abundances of baryons, cold dark matter, dark energy, photons, and neutrinos, where $\omega_i \equiv \rho_{i,0}/3H_{100}^2 M_{\text{pl}}^2$. We assume a flat Universe and parametrize the Hubble constant by $H_0 = h \cdot 100 \text{ Mpc}^{-1} \text{ km/s} \equiv h H_{100}$. Throughout this work, we fix the summed mass of neutrinos to $M_\nu \equiv \sum_i m_{\nu_i} = 0.06 \text{ eV}$, implemented as one massive neutrino species while all other light relics (both the fluidlike and remaining free-streaming ones) are massless. When varying the total radiation density N_{tot} , we ignore the SM prediction for the relic neutrino abundance; when instead studying

additional fluidlike (ΔN_{fld}) or free-streaming (ΔN_{fs}) light relics, we do fix the density of SM neutrinos to this prediction, treating them as 3.044 effective degrees of freedom that freely stream.

Throughout this work, we use the ultrarelativistic fluid species (parametrized by `N_ur`) implemented in the Boltzmann solver `CLASS 3.2.3` [42–44] to model fluidlike radiation. We set the effective sound speed squared and effective viscosity parameter to $c_{\text{eff,ur}}^2 = 1/3$, and $c_{\text{visc,ur}}^2 = 0$, respectively, which is a standard parametrization for a perfect fluid [45]. Note that the ultrarelativistic fluid approximation, which is implemented in `CLASS` to optimize the modeling of free-streaming radiation at late times, assumes that $c_{\text{visc,ur}}^2 = 1/3$. This approximation must therefore be disabled (by setting the parameter `ur_fluid_approximation` to 3) to accurately model a perfect fluid. We model the standard neutrino content with the implementation of non-cold dark matter species (`N_ncdm`). In the remainder of this section, we present a mix of analytic and numerical results. Numerical degeneracy directions are derived using CMB temperature and polarization data from the *Planck* PR4 analysis. We describe the datasets, priors, and methods we employ in Section 3.

2.1 Varying radiation density at fixed free-streaming fraction

We first review the extent to which the parameter freedom of standard Λ CDM can compensate for the effects of varying the total radiation density on the primary CMB anisotropies. The photon density ω_γ is measured to extremely high precision via direct measurements of the blackbody distribution [46, 47], leaving ω_r free to vary via N_{tot} [Eq. (2.1)]. In contrast to prior work, we fix f_{fs} in this analysis (by adjusting both N_{fs} and N_{fld} simultaneously) to isolate the variation of the total density in radiation from the changes to the dynamics of its perturbations [20, 21]. We first review the parameter combinations that are best constrained by CMB and therefore should be held fixed as the radiation density varies, resulting in specific degeneracy directions between the radiation density and other cosmological parameters. Differences in CMB anisotropies that persist along these degeneracy directions are attributed to changes in the pressure-supported fraction of matter [40, 48].

The CMB’s sensitivity to ω_b comes from the equilibrium point between gravitational collapse and radiation pressure in the pre-recombination plasma. The ratio of the heights of odd peaks (modes that have compressed) and even peaks (modes that have rarefacted) thus effectively measures the ratio of energy density in photons and baryons, commonly quantified as $R(a) = 3\rho_b/4\rho_\gamma = a3\omega_b/4\omega_\gamma$ where a is the scale factor. Since we fix ω_γ , we keep ω_b fixed for now.

The CMB probes the sum of the baryon and dark matter density $\omega_{cb} \equiv \omega_c + \omega_b$ via the scale factor of matter-radiation equality, $a_{\text{eq}} = \omega_r/\omega_{cb}$. Modes of the primordial plasma that enter the horizon during the radiation era are driven by the decay of the gravitational potentials, referred to as the radiation driving effect [41]. The onset of potential decay at horizon crossing coincides with the first oscillation of the plasma and therefore boosts the amplitude of these modes. But modes that enter the horizon when matter dominates more of the energy budget experience less driving. Therefore, the onset of matter domination determines the impact of radiation driving as a function of scale. This “radiation driving envelope” is sensitive to the fraction of density in radiation over a wide range of redshifts and has a distinct impact on CMB anisotropies [49]. When varying the radiation density, fixing a_{eq} via a proportional change to ω_{cb} (by adjusting ω_c , when ω_b is fixed) thus isolates the other effects of extra radiation from the well-measured radiation driving effect.

The angular positions of the acoustic peaks of the CMB are precisely quantified by the angular size of the sound horizon,

$$\theta_s \equiv r_{s,\star}/D_{M,\star}, \quad (2.4)$$

where $r_{s,\star}$ is the comoving sound horizon at recombination and $D_{M,\star}$ is the comoving distance to the surface of last scattering. Current data constrain θ_s with subpermille precision [1]. The comoving sound horizon is given by

$$r_{s,\star} = \int_0^{a_\star} da \frac{c_s(a)}{a^2 H} = \int_0^{a_\star} da \frac{c/\sqrt{3[1+R(a)]}}{H_{100}\sqrt{\omega_r + a\omega_{cb} + a^4\omega_\Lambda}}, \quad (2.5)$$

where $c_s(a) = c/\sqrt{3[1+R(a)]}$ is the sound speed of the plasma and a_\star the scale factor at recombination. At such high redshifts ($a \leq a_\star \approx 1/1100$), the contribution from dark energy is negligible. The sound horizon may then be written in terms of a_{eq} as

$$r_{s,\star} = \frac{c}{H_{100}\sqrt{\omega_r}} \int_0^{a_\star} da \frac{1/\sqrt{3[1+R(a)]}}{\sqrt{1+a/a_{\text{eq}}}}. \quad (2.6)$$

In a Universe with zero mean spatial curvature, the comoving distance to the surface of last scattering is

$$D_{M,\star} = \int_{a_\star}^1 da \frac{c}{a^2 H} = \int_{a_\star}^1 da \frac{c}{H_{100}\sqrt{\omega_r(1+a/a_{\text{eq}}) + a^4\omega_\Lambda}}, \quad (2.7)$$

to which radiation makes only a small contribution.¹ In a flat Universe with $a_{\text{eq}} = \omega_r/\omega_{cb}$ and ω_b (via R) held constant, fixing θ_s sets the dark energy density ω_Λ (or equivalently the Hubble parameter h) as a function of ω_r —specifically, requiring that $h \propto \sqrt{\omega_r}$.

The parameters that remain unspecified are those that determine the curvature power spectrum at the end of inflation and reionization at late times. We take a standard parametrization of the primordial power spectrum,

$$\Delta_{\mathcal{R}}^2(k) = A_s \left(\frac{k}{k_p} \right)^{n_s + \alpha_s \ln(k/k_p)/2 - 1}, \quad (2.8)$$

where A_s , n_s , and α_s are the amplitude, tilt, and running of the spectrum, and k_p is a pivot scale conventionally fixed to $k_p = 0.05 \text{ Mpc}^{-1}$. Except where explicitly stated otherwise, we fix the running α_s to zero.

Varying ω_r adjusts the size of physical scales, but CMB anisotropies measure the power spectrum as a function of angular scale. Since θ_s is effectively fixed by current data (compared to the precision on all other cosmological parameters), the CMB more directly measures the power in the mode that crosses the horizon at recombination, whose wave number is $k_{s,\star}$, rather than any fixed scale like k_p . Scaling A_s to hold $A_s(k_{s,\star}/k_p)^{n_s(k)-1}$ constant across cosmologies thus preserves the initial power at any given angular scale. Reionization also suppresses the observed amplitude of CMB anisotropies as $A_s e^{-2\tau_{\text{reio}}}$, where τ_{reio} is the optical

¹Note that by substituting $\omega_m = \omega_{cb} = \omega_r/a_{\text{eq}}$ in Eq. (2.7), we've ignored any additional contributions to the matter density at late times from, e.g., massive neutrinos. In this work we fix the sum of neutrino masses to the minimum, 0.06 eV; the corresponding contribution to the late-time matter density of about half a percent is safely ignorable for these analytic estimates.

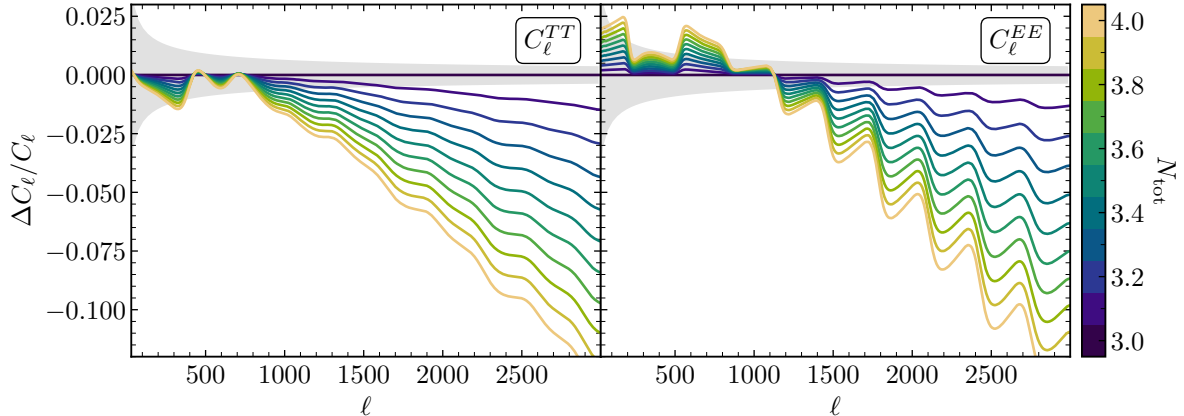


Figure 1. Impact of varying the total radiation density ω_r (i.e., N_{tot}) at fixed free-streaming fraction f_{fs} on the unlensed temperature and E -mode polarization power spectra. Results are displayed as the relative differences from a reference cosmology with $N_{\text{tot}} = 3$. Other Λ CDM parameters are adjusted to fix θ_s , a_{eq} , and the initial power in the mode that crosses the horizon at recombination (with wave number $k_{s,*}$). The primordial helium mass fraction is fixed to the BBN prediction in these cosmologies. The grey shaded region shows the extent of cosmic variance for observations spanning a sky fraction $f_{\text{sky}} = 0.8$ binned by multipole in intervals $\Delta\ell = 30$.

depth to reionization, which we fix in this discussion as it is independently constrained by CMB polarization on large scales.

To isolate the dependence of the CMB on the total amount of radiation ω_r/ω_γ (i.e., N_{tot}) from changes to its composition, we vary the total radiation density by adding both fluidlike and free-streaming radiation to fix f_{fs} to its Λ CDM value of 0.4087. The remaining freedom in Λ CDM parameters is used to preserve the aforementioned effects: we fix $100\omega_b = 2.2218$, $z_{\text{eq}} = 3411$ (by adjusting ω_c), $100\theta_s = 1.04075$ (by adjusting ω_Λ), $\tau_{\text{reio}} = 0.0517$, and $n_s = 0.9635$. We scale A_s to fix $\Delta_{\mathcal{R}}^2(k_{s,*})$ (taking $A_s = 2.0801 \times 10^{-9}$ as a reference value). Figure 1 shows the effect of increasing N_{tot} on both the temperature and polarization power spectra, subject to these choices. At $\ell \lesssim 1000$, the differences in the temperature spectra are incurred by changes in the pressure-supported matter fraction (ω_b/ω_{cb}), which we discuss further in Section 2.3. While this effect is also relevant on these scales in the polarization spectra, polarization is further enhanced because the width of the visibility function relative to the Hubble rate increases [50, 51], arising from detailed changes to the ionization history as the rate of Thomson scattering per e -fold $d\kappa/d\ln a \equiv n_e\sigma_T/H$ depends on ω_r . (Here n_e is the number density of free electrons and σ_T the cross-section of Thompson scattering.)

At smaller scales ($\ell \gtrsim 1000$), on the other hand, both the temperature and polarization spectra in Fig. 1 are suppressed by additional radiation. This scale-dependent suppression is due in part to the broadening of the visibility function [50–52], but more so due to Silk damping [40]. Perturbations of the photon distribution on scales smaller than the mean free path of photons during recombination are exponentially damped by a factor of $e^{-(k/k_D)^2}$, where

$$k_D^{-2} = \int_0^{a_*} \frac{da/a}{(aH)^2} \left(\frac{n_e\sigma_T}{H} \right)^{-1} \frac{R^2 + 16(1+R)/15}{6(1+R)^2} \quad (2.9)$$

is the wave number associated with the mean squared diffusion distance at decoupling [50, 52]. As established above, the shape of the acoustic peaks motivate fixing ω_b and a_{eq} , choices for

which $R(a)$ and $H(a)/H(a_*)$ are fixed as functions of a/a_* . Then, the variation of k_D with ω_r (beyond scaling with a_*H_*) is determined by the dimensionless Thomson rate $d\kappa/d\ln a$ [51]. Thomson scattering per e -fold decreases in a Universe that expands faster (due to additional radiation), allowing photons to diffuse further and increasing the damping of small-scale anisotropies. As evident in Fig. 1, high-resolution CMB observations are quite sensitive to the angular scale of diffusion, $\theta_D = r_D/D_{M,*}$, written in terms of the diffusion length $r_D = 2\pi/k_D$.

To study the parameter dependence of $d\kappa/d\ln a$, note that most of the photon diffusion that damps small-scale anisotropies occurs during the last e -fold before last scattering, between helium and hydrogen recombination. In this period, the number density of free electrons is $n_e(a) = x_e(a)(1 - Y_{\text{He}})\rho_b/m_{\text{H}}$, where $x_e = n_e/n_{\text{H}}$ is the hydrogen ionization fraction and $Y_{\text{He}} \equiv \rho_{\text{He}}/\rho_b$ the primordial fraction of baryons in helium by mass. Calculations of Big Bang nucleosynthesis (BBN) in the SM predict the helium yield as a function of the baryon-to-photon ratio and the radiation density (i.e., N_{tot}); treating Y_{He} as a free parameter is a commonly considered means to compensate for the impact of additional radiation on diffusion damping [40]. Were the ionization history a fixed function of a/a_* , the diffusion length relative to the sound horizon would be fixed by taking $1 - Y_{\text{He}} \propto \sqrt{\omega_r}$ (which fixes the Thomson rate per e -fold). But the ionization history is appreciably modified by variations in ω_r and Y_{He} , with nonnegligible impact on the parameter dependence [51], which we determine numerically to be

$$r_D/r_s \propto \frac{\omega_r^{0.134}}{(1 - Y_{\text{He}})^{0.238}}. \quad (2.10)$$

In the SM, the BBN prediction scales approximately as $1 - Y_{\text{He}} \propto \omega_r^{-0.13}$ [53, 54], which compounds slightly with the scaling of r_D/r_s at fixed Y_{He} and exacerbates the impact of varying the radiation density on diffusion damping.

Small-scale damping provides most of the constraining power on ω_r , but freedom in additional beyond- Λ CDM parameters, like Y_{He} as in Eq. (2.10), could conceal this effect. We next discuss two avenues that compensate for the increase in diffusion damping: adjusting Λ CDM parameters beyond the degeneracies discussed in this section (Section 2.1.1) and introducing additional freedom in the primordial power spectrum (Section 2.1.2) or the primordial helium yield (Section 2.1.3).

2.1.1 Tilt degeneracy

The impact of diffusion damping at large ℓ can be partially compensated for by changes to Λ CDM parameters, though at the expense of altering the other, aforementioned physical effects (and possibly degrading the fit) at low ℓ . For instance, one could modify the scale dependence of the initial conditions and/or the dynamics of the photon-baryon plasma in the radiation era—namely, the scalar tilt n_s and the baryon density ω_b [55, 56].

First, the scale-dependent suppression from diffusion may be compensated for with a bluer initial power spectrum, i.e., larger n_s . Since the conventional pivot scale corresponds to a multipole of $\ell_p = k_p/D_{M,*} \approx 700$, anisotropies at lower multipoles (around the first two acoustic peaks) are suppressed. In turn, the first peak may be boosted by increasing ω_b (i.e., R): an increase in so-called baryon loading shifts the zero point of the acoustic oscillations, enhancing the relative peak heights. Increasing the baryon density itself also partly offsets the increased diffusion rate: from Eq. (2.9), the diffusion scale increases with R , pushing the impact of damping to smaller scales.

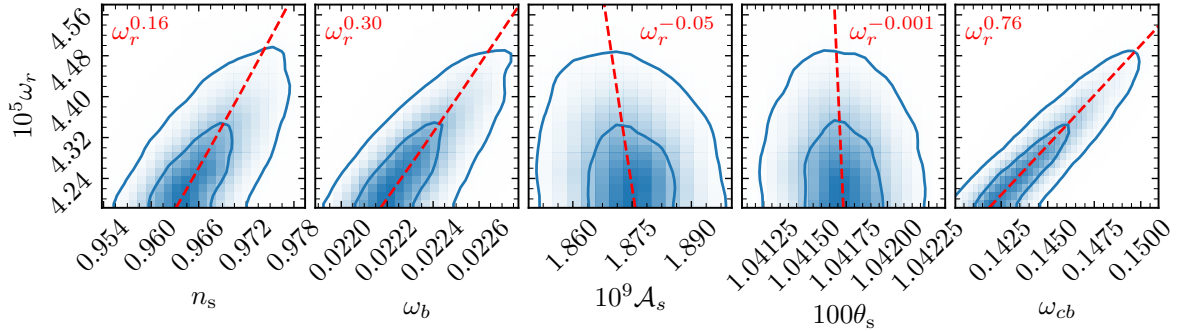


Figure 2. Joint posterior distributions between the total radiation density ω_r and n_s , ω_b , $\mathcal{A}_s \equiv A_s e^{-2\tau_{\text{reio}}}$, θ_s , and ω_{cb} , holding f_{fs} fixed and using the *Planck* 2020 TT, TE, and EE high- ℓ likelihood (CamSpec), the *Planck* 2020 low- ℓ EE likelihood (LoLLiPoP), and the *Planck* 2018 low- ℓ TT likelihood. The tilt degeneracy directions, determined via numerical fits, appear in dashed red and are labeled on each panel. Here Y_{He} is fixed to the BBN prediction as a function of ω_b and ω_r .

The competition between these effects—changes to the relative peak heights and the small-scale suppression due to diffusion—ultimately depends on the relative precision of measurements at large and small scales for any set of CMB observations, insofar as they determine parameter constraints. To investigate the relationship between these parameters as constrained by *Planck* PR4 CMB data, Fig. 2 presents joint posterior distributions (and numerical estimates of degeneracy directions) of Λ CDM parameters with N_{tot} , fixing the free-streaming fraction to $f_{\text{fs}} = 0.4087$. These results consistently set Y_{He} to the Big Bang Nucleosynthesis (BBN) prediction, assuming the extra radiation is also present during nucleosynthesis. (Since we do not change the density in photons, fixing the free-streaming fraction does not allow for ω_r lower than its standard value, $\omega_\gamma/f_{\text{fs}}$.)

For the posteriors in Fig. 2 deriving from *Planck* PR4 data, we empirically find that

$$n_s|_{f_{\text{fs}}} \propto \omega_r^{0.16}, \quad (2.11a)$$

$$\omega_b|_{f_{\text{fs}}} \propto \omega_r^{0.30}. \quad (2.11b)$$

Since varying the radiation density at fixed a_{eq} and f_{fs} does not alter the propagation of acoustic waves in the plasma, ω_r shows no notable correlation with $\mathcal{A}_s \equiv A_s e^{-2\tau_{\text{reio}}}$ and θ_s . Notably, the matter density exhibits a slightly shallower correlation with ω_r than would fully fix a_{eq} , due to the competing effect of changing the pressure-supported matter fraction, ω_b/ω_{cb} . However, the relationships in Eq. (2.11) are only slightly modified when extracted from the subset of the posteriors in Fig. 2 for which a_{eq} differs by no more than half a percent from its best-fit value in Λ CDM. Since this similarity suggests that the signatures controlled by the pressure-supported matter fraction are effectively independent, we therefore take a_{eq} fixed when referring to the tilt degeneracy below. We discuss the pressure-supported matter fraction in Section 2.1.3, where we promote Y_{He} to a free parameter to compensate for the effects of radiation on small-scale damping. For now, we focus on the correlations of n_s and ω_b with ω_r .

Figure 3 illustrates the variation in the CMB spectra along the tilt degeneracy. The relative precision of *Planck* data at small and large ℓ controls the extent to which the tilt degeneracy is viable. We compare cosmologies with $N_{\text{tot}} = 3.044$ (the SM prediction) and 3.58 (the 95th percentile of the posterior in Fig. 2). Adjusting n_s alone offsets some of the impact on the damping tail but also suppresses the first acoustic peak. Additionally adjusting

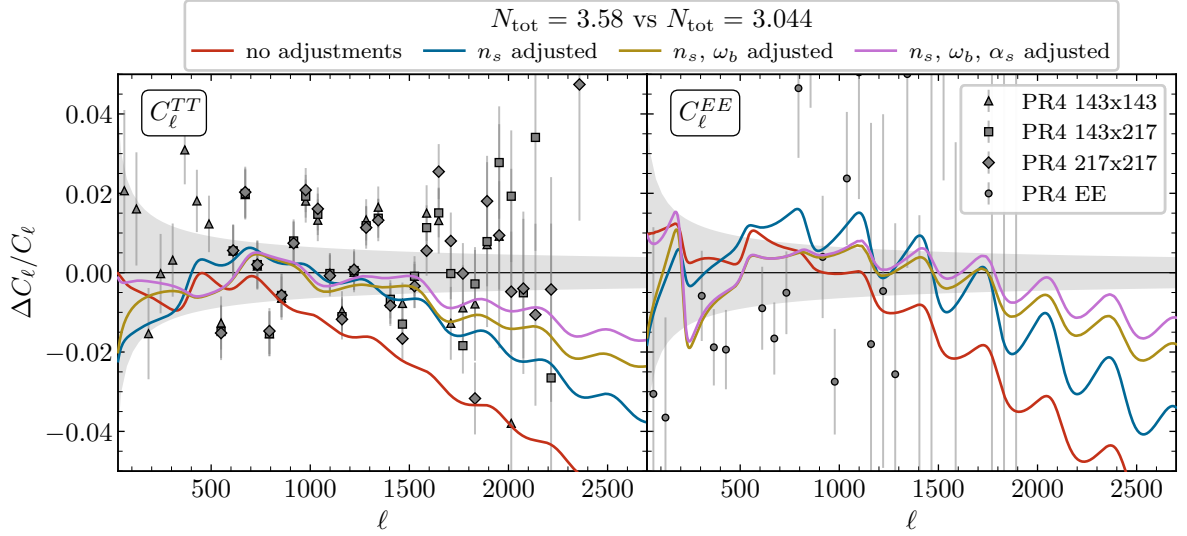


Figure 3. Illustration of the tilt degeneracy [Eq. (2.11)], displaying residuals of the lensed temperature and E -mode polarization power spectra for cosmologies with $N_{\text{tot}} = 3.58$ relative to one with $N_{\text{tot}} = 3.044$. The red, blue, and gold curves respectively adjust no parameters, n_s alone, and both n_s and ω_b according to Eq. (2.11). The purple curve additionally adjusts α_s as in Eq. (2.12). Other parameters are specified as in Fig. 1. The grey shaded region shows the extent of cosmic variance for observations spanning a sky fraction $f_{\text{sky}} = 0.8$ binned by multipole in intervals $\Delta\ell = 30$, and the binned *Planck* 2020 spectra and uncertainties are superimposed for the 143×143 GHz (triangle), 143×217 GHz (square), and 217×217 GHz (diamond) temperature maps, along with the polarization map (circle), where all frequencies and their cross-spectra have been co-added [57].

ω_b slightly increases the first peak and also further mitigates the enhanced damping on small scales.

2.1.2 Running of the spectral tilt

Beyond the scalar spectral tilt n_s , the running α_s provides additional freedom with which to compensate for damping induced by additional radiation without altering dynamics. In addition to the tilt degeneracy [Eq. (2.11)], for the same set of *Planck* PR4 data we empirically find that the posterior is oriented best along the line

$$\alpha_s|_{f_{\text{is}}} \propto 3984\omega_r, \quad (2.12)$$

since α_s is constrained close to zero. The impact of adjusting α_s is also illustrated in Fig. 3. Similar to n_s , α_s offsets impacts to the damping tail but, unlike n_s , can simultaneously improve the fit at larger scales.

2.1.3 Degeneracy with the helium fraction

As seen in the tilt degeneracy, the standard Λ CDM model only has sufficient freedom to partially compensate for the radiation density's impact on diffusion damping. Figure 4 shows that fixing θ_D by varying Y_{He} [according to Eq. (2.10)] largely removes the small-scale suppression incurred by larger radiation densities. The remaining residuals derive from the change to the fraction of the matter density that is pressure supported (ω_b/ω_{cb}) [40, 48], since fixing both a_{eq} and R with increasing ω_r requires holding ω_b constant and increasing

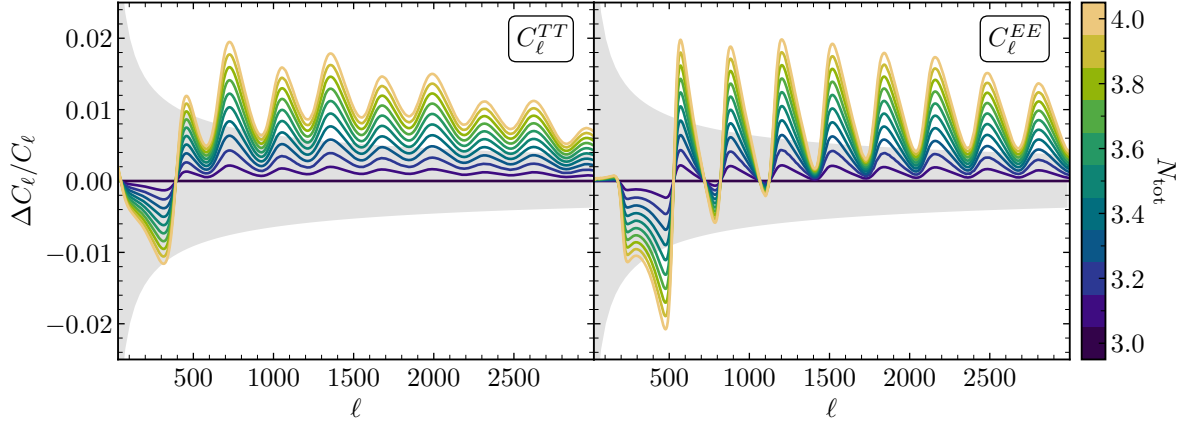


Figure 4. Impact of varying the total radiation density ω_r (i.e., N_{tot}) on the unlensed temperature and E -mode polarization power spectra, fixing the free-streaming fraction and the angular scale of diffusion $\theta_D = 3.23 \times 10^{-3}$ (by adjusting the Helium mass fraction Y_{He}) as well as θ_s , a_{eq} , and $\Delta_{\mathcal{R}}^2(k_{s,*})$ as in Fig. 1. The latter controls for the impact of larger radiation densities on small-scale damping, leaving the fraction of the matter density that is pressure supported as the most significant variable remaining. Results are presented as in Fig. 1.

ω_c . Gravitational potentials then decay to a lesser extent in the radiation era, with twofold (and scale-dependent) effects on acoustic oscillations. First, the radiation driving effect is diminished for large-scale modes (those that undergo no more than a single oscillation), reducing the amplitude of photon perturbations around the first acoustic peak ($\ell \lesssim 400$ in Fig. 4). However, smaller-scale modes that oscillate multiple times before last scattering do so in deeper potential wells, in which they compress to higher densities. CMB anisotropies are thus enhanced on the smaller angular scales that are primarily sourced by these modes, as evident in Fig. 4. We discuss this effect in connection to the dynamics of radiation perturbations in Section 2.3.1.

2.2 Varying free-streaming fraction at fixed radiation density

Section 2.1 considers the degeneracies of the total radiation density ω_r with other cosmological parameters while fixing its composition—that is, the fraction thereof that freely streams (f_{fs}). These degeneracies depend largely on the background cosmology rather than the dynamics of its perturbations. We now review the impact of the composition of radiation at fixed density (N_{tot}), following Refs. [20, 21].

The effect of free-streaming radiation can be understood analytically in the radiation-dominated epoch by expanding in small f_{fs} to study how differences in the gravitational potential sourced by the anisotropic stress of free-streaming radiation modify the monopole of the photon distribution. This correction to the Sachs-Wolfe effect imprints in the amplitude and the location of the extrema of the CMB spectra. The analytic prediction in the radiation-dominated era for the ratio of the amplitudes of the temperature and polarization spectra between first and zeroth order is [20, 21]

$$\frac{C_\ell^{(1)}}{C_\ell^{(0)}} = (1 - 0.268 f_{\text{fs}})^2, \quad (2.13)$$

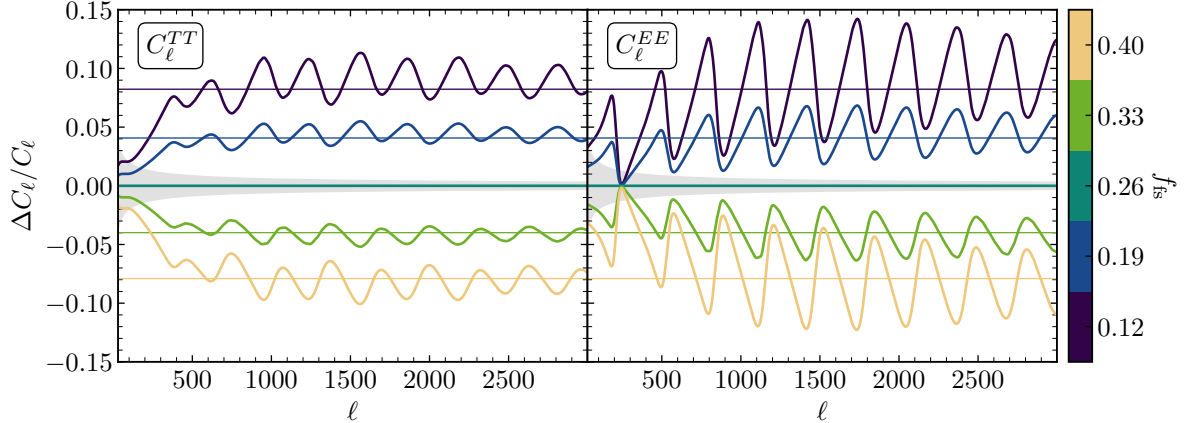


Figure 5. Impact of varying the free-streaming fraction f_{fs} on the unlensed CMB temperature and polarization power spectra at fixed $N_{\text{tot}} = 3$, changing no other cosmological parameters (i.e., holding the background cosmology fixed). Residuals are computed relative to a cosmology with $f_{\text{fs}} = 0.26$ for illustration. Results are depicted as in Fig. 1. The only physical difference is in the dynamics of radiation perturbations; in contrast to, e.g., Fig. 4, the fraction of pressure-supported matter does not vary. The colored horizontal lines correspond to the analytic prediction for the amplitude shift with f_{fs} [Eq. (2.13)].

and the acoustic peaks shift in multipole by

$$\delta\ell \approx -0.19 f_{\text{fs}} \Delta\ell, \quad (2.14)$$

where $\Delta\ell \approx \pi/\theta_s \approx 300$ is the average separation between the peaks [58].

Figure 5 illustrates these physical effects for cosmologies with f_{fs} varied at fixed $N_{\text{tot}} = 3$ to remove the effects of extra radiation density on the background cosmology (Section 2.1). The offset in amplitude matches Eq. (2.13) well at $\ell \gtrsim 700$, corresponding to modes for which the approximation of radiation domination is accurate. The oscillations of the residuals about Eq. (2.13) increase in amplitude for greater changes in f_{fs} due to the increased phase shift [Eq. (2.14)]. The effect of changing f_{fs} gradually diminishes in the matter era, as radiation’s relative contribution to the Einstein equations decreases. The residuals in Fig. 5 therefore decrease at lower multipoles—those dominated by scales that only become dynamical around or after matter-radiation equality. We discuss the scale dependence of these effects further in Section 2.3.1.

2.2.1 Shift degeneracy

Since the free-streaming fraction impacts both the amplitude and the location of the peaks of the spectra, it should be at least partially degenerate with $\mathcal{A}_s \equiv A_s e^{-2\tau_{\text{reio}}}$, which controls the overall amplitude of CMB anisotropies, and θ_s , which is determined by the location of the peaks [21, 26, 58]. To investigate the relationship between f_{fs} and other Λ CDM parameters, Fig. 6 presents study posteriors deriving from *Planck* PR4 CMB data in models where the free-streaming fraction is allowed to vary but the total amount of radiation is fixed to $N_{\text{tot}} = 3.044$. Since we do not alter the photon density and N_{tot} is fixed, values of f_{fs} above the SM prediction of $f_{\text{fs}} = 0.4087$ are disallowed. As anticipated [20, 21], we empirically find a strong degeneracy between f_{fs} , \mathcal{A}_s , and θ_s . We coin this partial numerical degeneracy a “shift degeneracy” to differentiate from the tilt degeneracy (Section 2.1.1) due to the effects

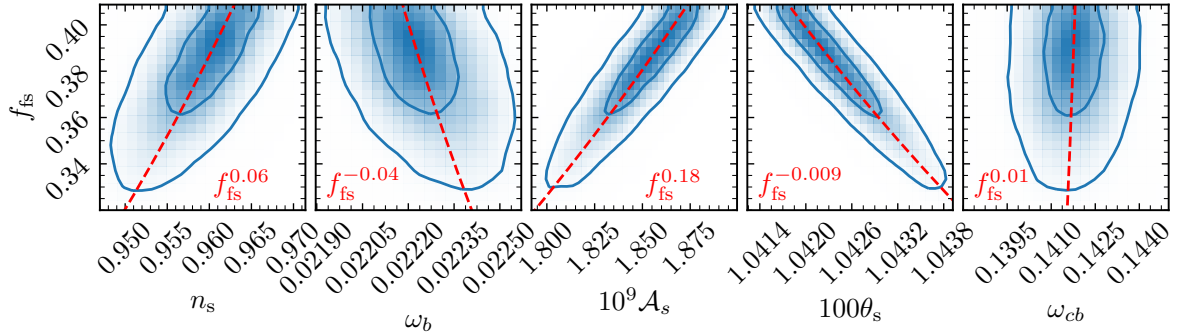


Figure 6. Joint posterior distribution between the free-streaming fraction f_{fs} and n_s , ω_b , \mathcal{A}_s , θ_s , and ω_{cb} . Results fix $N_{\text{tot}} = 3.044$ and use the *Planck* 2020 TT, TE, and EE high- ℓ likelihood (CamSpec), the *Planck* 2020 low- ℓ EE likelihood (LoLLiPoP), and the *Planck* 2018 low- ℓ TT likelihood. The tilt degeneracy directions, determined via numerical fits, appear in dashed red and are labeled on each panel. Here Y_{He} is fixed to the BBN prediction as a function of ω_b .

of the radiation density on the background cosmology. We also find mild correlations with ω_b and n_s , which can both partially mitigate the effects of varying f_{fs} on the first peak (see Fig. 5). Unlike for a varying radiation density, for which a proportional increase in ω_{cb} fixes a_{eq} , there is little correlation between f_{fs} and ω_{cb} . For the posteriors in Fig. 6 deriving from *Planck* PR4 data, we empirically find that

$$\mathcal{A}_s|_{\omega_r} \propto f_{\text{fs}}^{0.18}, \quad (2.15a)$$

$$\theta_s|_{\omega_r} \propto f_{\text{fs}}^{-0.0090}, \quad (2.15b)$$

$$n_s|_{\omega_r} \propto f_{\text{fs}}^{0.06}, \quad (2.15c)$$

$$\omega_b|_{\omega_r} \propto f_{\text{fs}}^{-0.04}. \quad (2.15d)$$

Note that while the correlation in Eq. (2.15b) appears weak, the exquisite precision of the measurement of θ_s makes it relevant. To illustrate this shift degeneracy, Fig. 7 shows the impact of each of θ_s , \mathcal{A}_s , n_s and ω_b on the CMB power spectra for $f_{\text{fs}} = 0.34$ (the 5th percentile of the posterior in Fig. 6) compared to a baseline cosmology with $f_{\text{fs}} = 0.41$. Adjusting θ_s compensates for the shift of the peaks, especially in the range $500 < \ell < 1500$, reducing the oscillations of the residuals in both temperature and polarization. Shifting \mathcal{A}_s accounts for the change in amplitude as predicted in Eq. (2.13). Finally, adjusting n_s tilts the spectra to better absorb the scale dependent amplitude change in the first peak while adjusting ω_b further decreases the amplitude in the first peak. We stress again that this partial degeneracy direction is a function of the precision of *Planck* observations, which are displayed in Fig. 7.

2.3 Free-streaming versus fluidlike radiation

We have thus far studied parameter degeneracies when varying the total radiation density at fixed free-streaming fraction and vice versa. Although ω_r and f_{fs} most cleanly encode the physical effects on cosmological observables, contributions from BSM physics are more conveniently parametrized through ΔN_{fs} and ΔN_{fld} , insofar as new degrees of freedom either freely stream or are fluidlike (and therefore modify ω_r and f_{fs} simultaneously). (We do not consider the possibility of sectors whose interactions decouple or recouple on cosmologically relevant timescales [15, 24, 27, 56, 59, 60].)

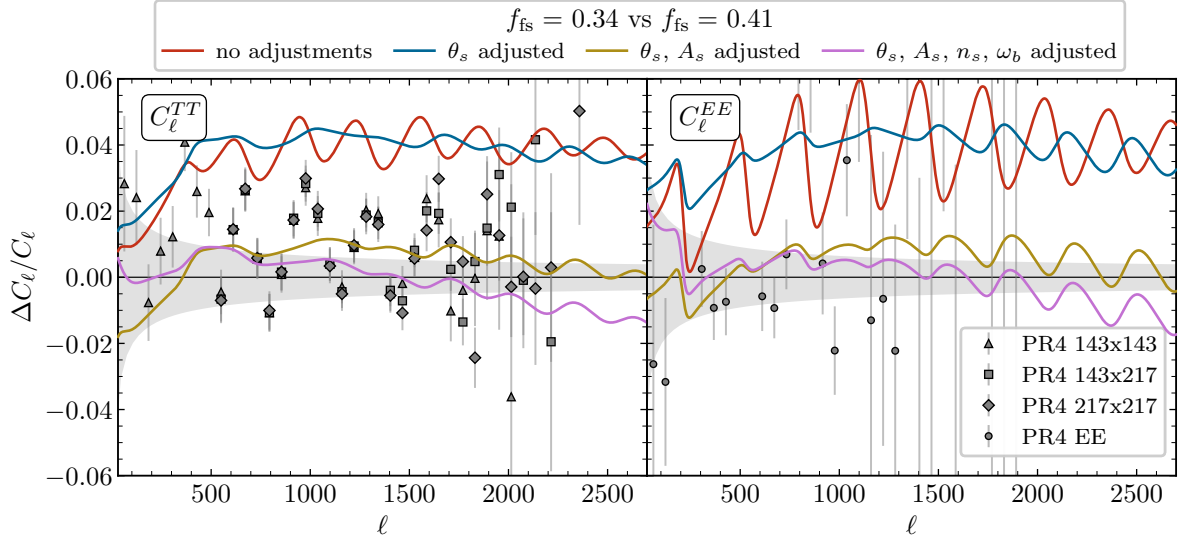


Figure 7. Illustration of the shift degeneracy [Eq. (2.15)], displaying residuals of the lensed temperature and E -mode polarization power spectra for cosmologies with $f_{\text{fs}} = 0.34$ relative to one with $f_{\text{fs}} = 0.41$. The red, blue, and gold curves respectively adjust no parameters, θ_s alone, and both θ_s and A_s according to Eqs. (2.15a) and (2.15b). The purple curve additionally adjusts n_s and ω_b as in Eqs. (2.15c) and (2.15d). All other parameters are fixed. Results are otherwise presented as in Fig. 3.

While equal increases in N_{fs} and N_{fld} yield the same total radiation density and therefore increase damping (Fig. 1) and decrease the fraction of matter that is pressure supported (Fig. 4) to the same extent, they change the free-streaming fraction by differing amounts and with opposite sign. To leading order,

$$\Delta f_{\text{fs}} \approx (1 - f_{\text{fs}}) \frac{\Delta \rho_{\text{fs}}}{\rho_r} - f_{\text{fs}} \frac{\Delta \rho_{\text{fld}}}{\rho_r}. \quad (2.16)$$

In the baseline cosmology where $\rho_{\text{fs}} = \rho_\nu$ and $\rho_r = \rho_\gamma + \rho_\nu$, the free-streaming fraction $f_{\text{fs}} \approx 0.4087$; effects that are controlled by the free-streaming fraction are then roughly $(1 - f_{\text{fs}})/f_{\text{fs}} \approx 1.45$ times greater in magnitude for an increase of ΔN_{fs} compared to an equal increase of ΔN_{fld} . When adjusting, e.g., Y_{He} in order to compensate for the common effect on small-scale damping and fixing parameters as in Section 2.1, the ultimate impacts of additional free-streaming and fluidlike radiation are differentiated by the interplay between their common change to the pressure-supported matter fraction and their distinct changes to the free-streaming fraction.

2.3.1 Interplay between free-streaming radiation and pressure supported matter

To study the impact of correlated changes to the free-streaming fraction and pressure-supported matter fraction, Fig. 8 displays residuals of the temperature and polarization spectra for cosmologies with $\Delta N_{\text{fs}} = 1$ and $\Delta N_{\text{fld}} = 1$ relative to the baseline case with $N_{\text{fs}} = 3.044$, fixing θ_s , ω_b , a_{eq} , and θ_D (by adjusting Y_{He}) as in Section 2.1.3. As discussed in Section 2.1, these choices effectively compensate for all effects that derive from changes to the expansion history. Figure 8 also presents results for commensurate changes to f_{fs} at fixed N_{tot} and vice versa.² Note that Ref. [48, see Fig. 3] also compared the signatures of extra fluidlike or

²In order to vary f_{fs} at fixed N_{tot} without modifying the photon density, we set $N_{\text{tot}} = 4$ in these cases and adjust other parameters to preserve the Λ CDM values of ω_b , θ_s , θ_D , and a_{eq} .

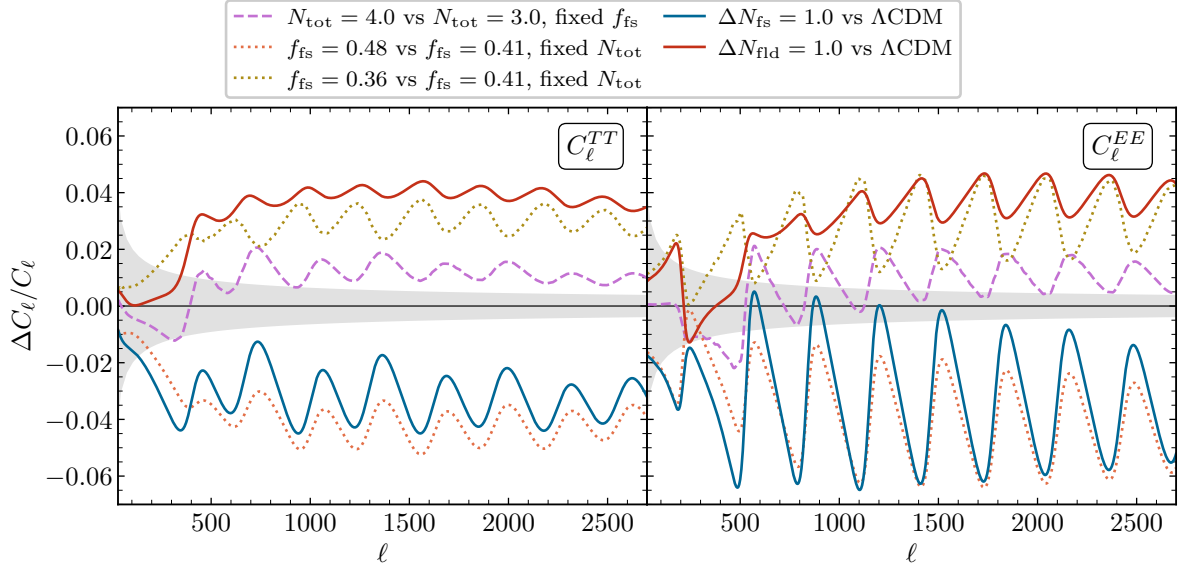


Figure 8. Impact of additional free-streaming versus additional fluidlike radiation on the unlensed CMB temperature (left) and polarization (right) power spectra, comparing residuals for cosmologies $\Delta N_{\text{fs}} = 1$ (blue) and $\Delta N_{\text{fld}} = 1$ (red) relative to the baseline cosmology. In both panels, purple dashed curves increase N_{tot} by one but fix f_{fs} ; by also fixing a_{eq} , θ_s , and θ_D , these results illustrate the isolated effect of changing the fraction of pressure-supported matter. Dotted curves show the effect of increasing (orange) or decreasing (gold) the free-streaming fraction by the same amount incurred by $\Delta N_{\text{fs}/\text{fld}} = 1$ while holding N_{tot} fixed. In all cases, a_{eq} , θ_s , θ_D , ω_b , A_s , and n_s are fixed as in Fig. 4; results are otherwise presented as in Fig. 1.

free-streaming radiation to the case with the same radiation density but fixed free-streaming fraction, interpreting the results relative to an expanded “mirror-world” dark sector scenario. In Fig. 8, we instead consider the complementary case with fixed radiation density and varying free-streaming fraction in order to explain the contrast in the combined effects for fluidlike and free-streaming light relics. We discuss three notable features in Fig. 8: signatures that are oscillatory in ℓ and impact the peak locations, the overall shift in amplitude at high ℓ , and the differing effects on the first peak ($\ell \lesssim 400$).

First, with additional free-streaming radiation the residuals of the temperature spectra exhibit oscillations in multipole that are comparable in amplitude to their average. By contrast, when adding fluidlike radiation the residuals’ oscillations at $\ell \gtrsim 500$ are about a tenth (rather than nearly half) of the size of the scale-independent shift. A similar comparison holds for polarization, but the residuals oscillate with roughly double the amplitude in all cases. Decreasing the pressure-supported matter fraction moves the peaks to slightly larger scales by shifting the zero-point of oscillations in the baryon-photon fluid. This effect adds constructively with the phase shift induced by increasing the free-streaming fraction with additional free-streaming radiation, while the two effects are out of phase with additional fluidlike radiation, exacerbating the oscillations in the former case and diminishing them in the latter. The resulting shifts in peak locations due to free-streaming and fluidlike radiation, listed in Table 1, therefore differ in magnitude by much more than 1.45 (and even in sign for the second and third peak), as predicted if ω_b/ω_{cb} were fixed.

Next, in contrast to the expected ratio of 1.45 from Eq. (2.16), Fig. 8 displays an overall shift in amplitude at high ℓ that is slightly *smaller* in magnitude for free-streaming radiation

	0	1	2	3	4	5	6
$N_{\text{fs}} = 3.044$	220.7	537.0	815.3	1130.6	1428.4	1740.9	2040.4
$\Delta N_{\text{fs}} = 1.0$	-1.3	-1.7	-2.7	-2.6	-3.0	-2.9	-3.3
$\Delta N_{\text{fld}} = 1.0$	0.2	-0.1	-0.1	0.3	0.4	0.5	0.7

Table 1. Peak locations (in multipole) of the CMB temperature spectrum in Λ CDM cosmology (top row) and the shift in locations for the $\Delta N_{\text{fs}/\text{fld}} = 1.0$ models depicted in Fig. 8 (second and third rows).

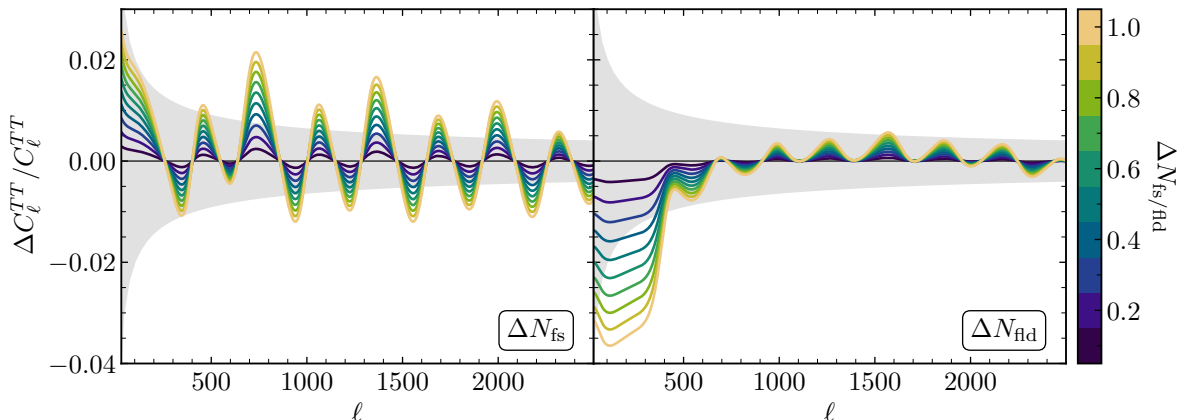


Figure 9. Illustration of the partial degeneracy between $N_{\text{fs}/\text{fld}}$, Y_{He} , and A_s in the CMB temperature spectra. Here A_s is chosen in each case to minimize the mean-squared difference (weighted by cosmic variance) of the temperature spectrum compared to the fiducial case with $N_{\text{fs}} = 3.044$ for $\ell > 1000$. Other cosmological parameters are adjusted to fix θ_s , θ_D , a_{eq} , ω_b , τ_{reio} , and n_s (see Section 2.1). Results are otherwise presented as in Fig. 1. Although not shown, the polarization spectra exhibit the same key features.

than that for fluidlike radiation. The results in Fig. 8 that vary f_{fs} at fixed N_{tot} on the other hand are indeed consistent with the expectation from Eq. (2.16). This reversal is due again to the common decrease of the fraction of matter that is pressure supported (ω_b/ω_{cb}), which Fig. 4 shows boosts power on small scales by a percent or so (for $\Delta N_{\text{tot}} = 1$), partly canceling the amplitude effect under additional free-streaming radiation and compounding with it for fluidlike radiation.

The interplay of these effects significantly impacts the degeneracy with the amplitude of the primordial power spectrum, A_s . From Eq. (2.13), to first order in f_{fs} , we expect an overall, fractional change in the amplitude of the CMB spectra at high multipole of $\Delta C_\ell(f_{\text{fs}})/C_\ell(f_{\text{fs}}) = -0.246\Delta f_{\text{fs}}/f_{\text{fs}}$, which in principle could be compensated for by an equal and opposite change $\Delta A_s/A_s$.³ To study the impact of the reduction in ω_b/ω_{cb} on degeneracies with the primordial amplitude, Fig. 9 varies $\Delta N_{\text{fs}/\text{fld}}$ (as usual, at fixed θ_s , a_{eq} , and θ_D) and adjusts A_s to compensate for the effects at high ℓ . We empirically determine the optimal relationship between A_s and f_{fs} by minimizing the cosmic-variance-weighted, mean-squared

³This prediction differs from the relationship observed between A_s and f_{fs} in the shift degeneracy (Fig. 6) due to the influence of low- ℓ data, which we discuss next. Figure 5 demonstrates that amplitude differences incurred by changing f_{fs} only asymptote to the analytic prediction for $\ell \gtrsim 700$.

deviation between the temperature spectra of cosmologies of increasing $\Delta N_{\text{fs/fld}}$ and ΛCDM (i.e., $N_{\text{fs}} = 3.044$) using the Nelder-Mead minimization algorithm. The optimized values of A_s approximately lie along

$$\Delta A_s/A_s = \begin{cases} 0.21 \Delta f_{\text{fs}}/f_{\text{fs}}, & \text{for varying } \Delta N_{\text{fs}} \\ 0.31 \Delta f_{\text{fs}}/f_{\text{fs}}, & \text{for varying } \Delta N_{\text{fld}} \end{cases} \quad (2.17)$$

which is shallower (steeper) than the degeneracy direction predicted above for free-streaming (fluidlike) radiation.

As in Fig. 8, the reduction in the pressure-supported matter fraction when increasing N_{fs} amplifies the acoustic oscillations on small scales, partially compensating for the reduction in amplitude incurred by increasing f_{fs} . Moreover, for the amplitudes that minimize the deviation at $\ell > 1000$, the residuals at almost all ℓ also oscillate about zero for the case of additional free-streaming radiation. For fluidlike radiation, on the other hand, the same optimization procedure is ineffective because of a more severe mismatch between the first acoustic peak and small-scale anisotropies. The right panel of Fig. 9 shows that while the optimization does indeed center the residuals on zero at high ℓ , it does so at the expense of a severely suppressed first peak in the temperature power spectrum. The same effect is evident in the polarization spectra.

The differing impacts on the first peak compared to larger ℓ derive from the transition to matter domination shortly before recombination, as the modes that contribute to it entered the horizon after equality and do not complete a full oscillation before recombination. As explained in Refs. [40, 48] and reviewed in Section 2.1, decreasing the fraction of pressure-supported matter suppresses the anisotropies on large scales but boosts them at $\ell \gtrsim 400$. Figure 10 illustrates the interplay of this effect and the increase (decrease) in the free-streaming fraction f_{fs} under additional free-streaming (fluidlike) radiation. Specifically, Fig. 10 depicts the differences in the dynamics of the Sachs-Wolfe term $\Theta_0 + \psi$ for various cosmologies (where Θ_0 is the monopole of the photon distribution and ψ the gravitational potential [61]), for wave number $k = 0.016 \text{ Mpc}^{-1}$, which contributes significantly to first acoustic peak. While the change to the pressure-supported matter fraction reduces the Sachs-Wolfe term at recombination in both cases, the differences incurred by changing f_{fs} have opposite sign. Both effects are similar in magnitude. When $\Delta N_{\text{fs}} > 0$, these two effects conspire together to reduce the first peak, while in the cosmology with additional N_{fld} the effects largely cancel.

In summary, the combined effects of changing the radiation density and free-streaming fraction yield degeneracies in CMB anisotropies that are qualitatively distinct when considering additional free-streaming or fluidlike radiation. Free-streaming radiation results in a reduction in amplitude that is more coherent across scales but with substantial oscillations about the overall shift. Fluidlike radiation instead incurs a boost in amplitude at $\ell \gtrsim 400$ that is greater in magnitude but has nearly negligible oscillations. In this case, however, the first peak is largely unaffected. The relative amplitude of the first and higher acoustic peaks thus plays a crucial role in breaking the degeneracy between N_{fld} , A_s , and Y_{He} . In Appendix A, we explore the manner in which low- ℓ data break this degeneracy by comparing constraints from mock, *Planck*-like data over all scales and restricted to small scales.

2.4 Breaking degeneracies with large scale structure

Sections 2.1 to 2.3 focus on searches for signatures of light relics in primary CMB anisotropies because of their unique sensitivity to the dynamics of spatial perturbations in the radiation

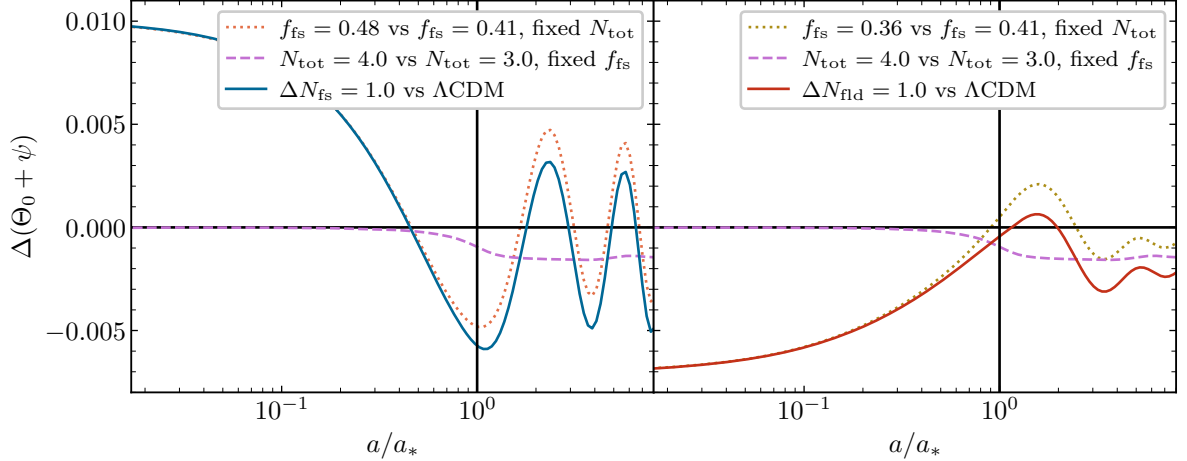


Figure 10. Differences in the evolution of the Sachs-Wolfe term $\Theta_0 + \psi$ for a mode that contributes significantly to the first peak of the CMB primary spectra. Solid curves compare models with $\Delta N_{\text{fs}} = 1$ (left, blue) and $\Delta N_{\text{fld}} = 1$ (right, red) to ΛCDM . In both panels, purple dashed curves increase N_{tot} by one but fix f_{fs} ; by also fixing a_{eq} , θ_s , and θ_D , these results illustrate the isolated effect of changing the fraction of pressure-supported matter. Dotted curves show the effect of increasing (left, orange) or decreasing (right, gold) the free-streaming fraction by the same amount incurred by $\Delta N_{\text{fs}/\text{fld}} = 1$ while holding N_{tot} fixed. For free-streaming radiation (left), the two effects each reduce the amplitude at recombination (indicated by the vertical black line), while with fluidlike radiation (right) their effects partially cancel.

epoch. But both the total radiation density (Section 2.1) and the free-streaming fraction (Section 2.2) remain degenerate to some degree with other cosmological parameters. These degeneracies can be broken by other observations, like the light element abundances and large-scale structure. The former—namely, astrophysical measurements of the primordial helium fraction, Y_{He} —break degeneracies in the damping tail with the total density N_{tot} . In the remainder of this section, we discuss the role large-scale structure observables, such as CMB lensing and the matter power spectrum, can play in breaking these degeneracies.

We first consider variations in N_{tot} at fixed f_{fs} , as studied in Section 2.1.1, again adjusting cosmological parameters to fix θ_s , a_{eq} , and θ_D (via Y_{He} as in Section 2.1.3). The remaining physical effect, the variation in the fraction of matter with pressure support (ω_b/ω_{cb}), increases power at high ℓ (Fig. 4), where the plasma oscillates in a deeper potential well (due to the increased relative importance of CDM). The same dynamics amplify large-scale structure, i.e., perturbations of the metric potentials and the matter density, as evident in Fig. 11. The relative increase in the CMB lensing and matter power spectra is around four times greater than that in the temperature and polarization spectra at large ℓ , which was at most 2% over the same range of N_{tot} (see Fig. 4). These observables can therefore independently break the amplitude degeneracy discussed in Section 2.3.1.

We next explore to what extent large-scale structure observations can independently break the tilt (Section 2.1.1) and shift (Section 2.2.1) degeneracies. Figure 12 presents the relative changes to the CMB lensing power spectrum and matter power spectrum in the same cosmologies considered in Figs. 3 and 7, which display the changes to the CMB temperature and polarization spectra. We compare cosmologies with $N_{\text{tot}} = 3.58$ and $f_{\text{fs}} = 0.34$ to ΛCDM for the tilt and shift degeneracies, respectively. None of the adjustments prescribed by the tilt degeneracy [Eq. (2.11)] abate the $\sim 3 - 4\%$ increase in power at $L \gtrsim 200$ in the lensing power

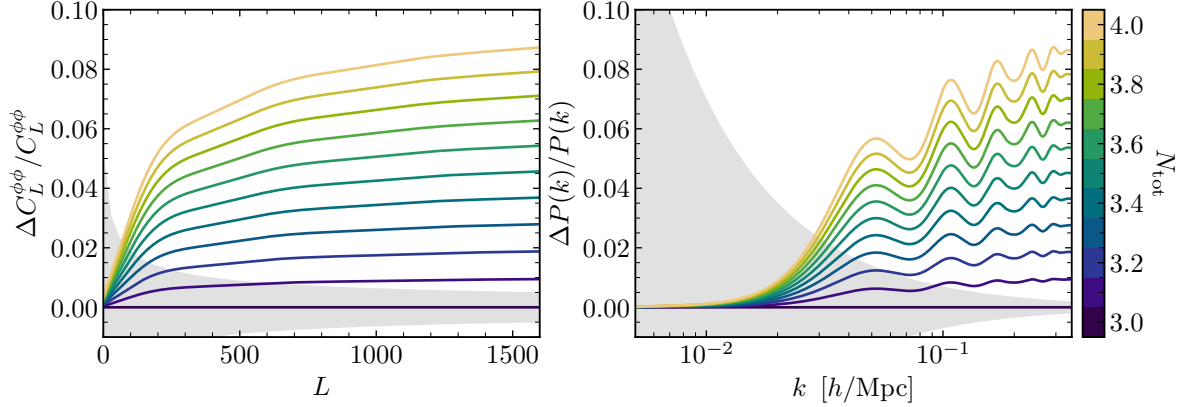


Figure 11. Impact of varying radiation density ω_r on the CMB lensing spectrum $C_\ell^{\phi\phi}$ (left) and the linear matter power spectrum $P_{mm}(k)$ (right) at fixed f_{fs} and θ_D (by varying Y_{He}). Other Λ CDM parameters are adjusted to fix θ_s , a_{eq} , and the initial power in the mode that crosses the horizon at recombination (with wave number $k_{s,*}$), as in Figs. 1 and 4. Residuals are computed relative to a cosmology where $N_{\text{tot}} = 3$. The grey bands depict cosmic variance for CMB lensing with $f_{\text{sky}} = 0.8$ binned with $\Delta\ell = 30$ (left) and for a survey volume of 20 Gpc^3 (right).

spectrum incurred by the increase in N_{tot} at fixed a_{eq} . In fact, the parameter adjustments of Eq. (2.11) increase the discrepancies at smaller scales in both CMB lensing and the matter power spectrum, albeit only moderately on linear scales. In contrast, both observables are less sensitive to changes in the free-streaming fraction, all else equal. However, adjusting A_s and n_s per the shift degeneracy [Eq. (2.15)] yield a pronounced impact on residuals, with differences again reaching the 5% level in the linear regime when all shift degeneracy parameters are adjusted. Figure 12 shows that, in addition to CMB lensing data, the full shape of the matter power spectrum could independently break the tilt and shift degeneracies deriving from current CMB data, along the lines of past work that considered self-interacting neutrinos [62, 63].

3 Constraints on dark radiation

We now apply the theoretical background of Section 2 to interpret the impact of the latest CMB and BAO data on parameter inference in dark-radiation scenarios. We begin in Section 3.1 by taking both N_{tot} and f_{fs} as free parameters, motivated by the discussion in Section 2 which phrases the physical origin of degeneracies with standard Λ CDM parameters in terms of the total radiation density ω_r and the fraction f_{fs} thereof that freely streams. In practice, for these models we vary the amount of both fluidlike and free-streaming radiation, ignoring the SM prediction for the contribution from neutrinos. To isolate the role of physical effects other than small-scale damping, we additionally study cases that allow Y_{He} to vary independently of its standard BBN prediction, as discussed in Section 2.1.3. We also consider varying the running of the scalar spectral index α_s (Section 2.1.2) as an alternative means to compensate for radiation’s impact on damping without altering dynamics (as impacted by Y_{He}). After studying general scenarios varying the total radiation density and its composition, in Section 3.2 we consider models featuring additional light relics (on top of SM neutrinos) that are either self-interacting (ΔN_{fld}) or free-streaming (ΔN_{fs}). In particular, we apply the results of Section 3.1 to understand any differential impact of particular datasets on

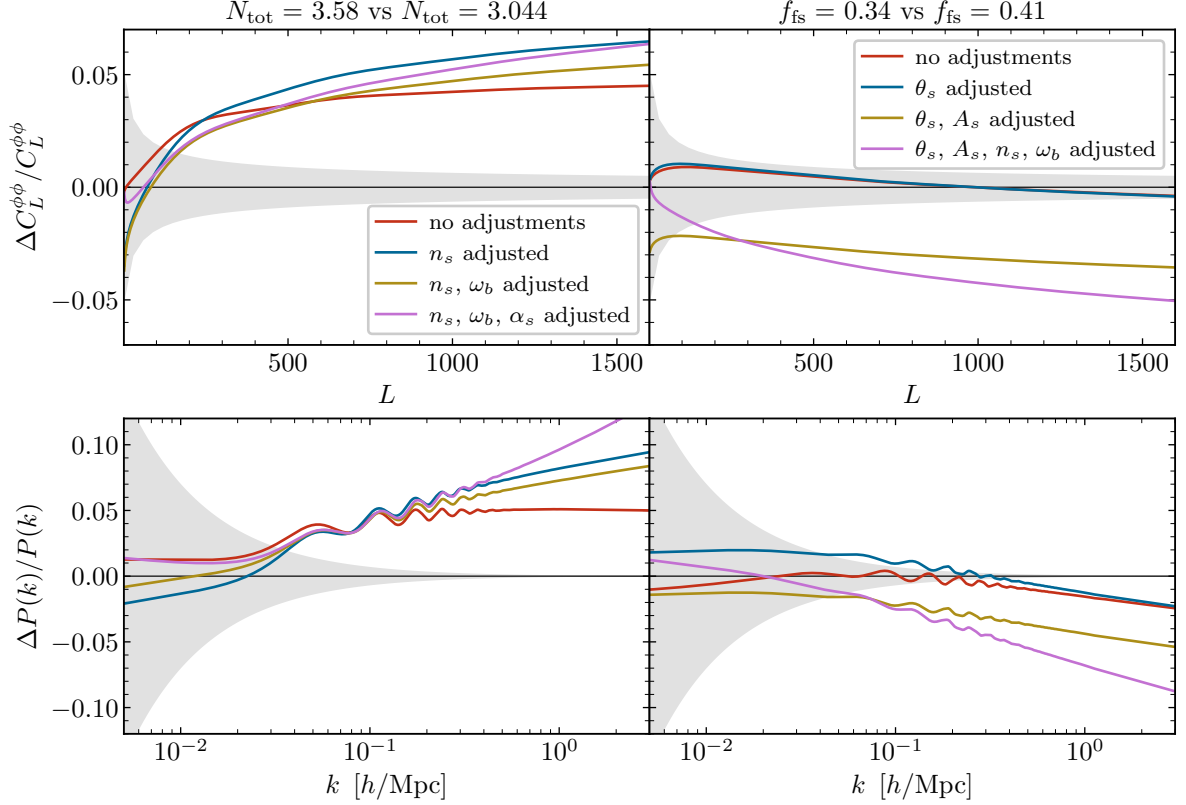


Figure 12. Relative changes to the CMB lensing potential power spectrum (top) and matter power spectrum (bottom) in cosmologies varying parameters along the tilt (left) and shift (right) degeneracies, comparing models with $N_{\text{tot}} = 3.58$ and 3.044 at fixed f_{fs} (left) and models with $f_{\text{fs}} = 0.34$ and 0.41 at fixed N_{tot} (right). Parameters are varied according to Eq. (2.11) (left) and Eq. (2.15) (right) as indicated on the legend; the CMB spectra for the corresponding cosmologies are displayed in Fig. 3 and Fig. 7, respectively. The grey bands depict cosmic variance as in Fig. 11.

parameter inference in each case (as derives from their opposite effects on the free-streaming fraction). Finally, in Section 3.3 we forecast parameter constraints from CMB-S4 [31] for all the aforementioned scenarios. Tables 2 to 5 in Appendix B tabulate constraints on other Λ CDM parameters for a number of the models and dataset combinations we consider.

To carry out the analyses in Sections 3.1 and 3.2 (and those presented in Figs. 2 and 6), we use the Boltzmann code CLASS 3.2.3 interfaced with cobaya 3.5.4 [64, 65]. We employ CMB temperature, polarization, and lensing data from *Planck*, considering both 2018 data via the nuisance-marginalized likelihoods [1, 66] (referred to as “PR3”) and subsequent reanalyses (“PR4”). Specifically, the latter uses the CamSpec likelihood [57] for data at $\ell \geq 30$, LoLLiPoP for *E*-mode data [32] and Commander for temperature data [66] at $\ell < 30$ (the latter of which employs 2018 data), and the PR4 lensing likelihood from Ref. [33]. The combinations PR3 and PR4 each include their respective lensing datasets unless otherwise specified, and in some cases we use the combined ACT DR6/*Planck* PR4 lensing dataset [34, 35]. Finally, we also study the impact of BAO observations either from DESI’s first data release [36–38] or from the Sloan Digital Sky Survey (SDSS), the latter including the Main Galaxy Sample from SDSS DR7 [67], the Baryon Oscillation Spectroscopic Survey (BOSS) DR12 galaxies [68], and the Extended BOSS (eBOSS) DR16 luminous red galaxies [69–71].

We sample posteriors using the `cobaya` implementation of the Metropolis-Hastings method for Markov chain Monte Carlo [72]. Denoting a uniform distribution between a and b as $\mathcal{U}(a, b)$, we take flat priors for Λ CDM parameters: $100\theta_s \sim \mathcal{U}(0.5, 10)$, $\omega_b \sim \mathcal{U}(0.005, 0.1)$, $\omega_c \sim \mathcal{U}(0.001, 0.99)$, $\ln(10^{10} A_s) \sim \mathcal{U}(1.61, 3.91)$, $n_s \sim \mathcal{U}(0.8, 1.2)$, and $\tau_{\text{reio}} \sim \mathcal{U}(0.01, 0.8)$. The total amount of radiation and the free-streaming fraction are sampled via $N_{\text{tot}} \sim \mathcal{U}(2.0, 4.5)$ and the ratio $N_{\text{fld}}/N_{\text{tot}} \sim \mathcal{U}(0, 1.0)$. When not otherwise fixed, we take $Y_{\text{He}} \sim \mathcal{U}(0.01, 0.5)$ and $\alpha_s \sim \mathcal{U}(-0.05, 0.05)$. For the cases considered in Section 3.2, we take ΔN_{fs} and $\Delta N_{\text{fld}} \sim \mathcal{U}(0, 1)$. We ensure that our presented results are robust to both thinning and the amount of samples dropped as burn-in. All posteriors presented contain between 4,000 and 11,000 independent samples, and we slightly smooth posterior contours to improve legibility without modifying their shape.

3.1 Impact of recent data on radiation density and composition

We first analyze the impact of recent datasets on constraints for models where both the radiation density and the free-streaming fraction vary, isolating what features of recent data are responsible for changes in parameter inference. Later (in Section 3.2) we apply this analysis to explain differences in constraints on additional free-streaming radiation or fluidlike radiation beyond the SM prediction. Figure 13 summarizes measurements on N_{tot} and f_{fs} for various dataset combinations in scenarios that fix Y_{He} to its BBN prediction, vary Y_{He} independently, and vary the running of the spectral index, α_s .

3.1.1 Planck PR3 versus PR4

The PR4 and PR3 data releases largely yield consistent inferences of Λ CDM parameters; in general, the PR4 release reduces parameter uncertainties by 10% to 20% [32, 57]. However, PR4 prefers slightly higher $N_{\text{fs}} = 3.08 \pm 0.17$ [57] compared to PR3 (2.92 ± 0.19 [1]), a result marginally closer to the SM prediction for $N_{\text{fs}} = 3.044$ for neutrinos. This preference for additional radiation persists in models where N_{tot} and f_{fs} both vary, as shown in Fig. 14. When fixing Y_{He} to its BBN prediction (as a function of N_{tot} and the baryon-to-photon ratio), the posteriors over N_{tot} from PR4 shift around half a standard deviation higher and also broaden marginally. When Y_{He} is instead taken as a free parameter, the posteriors are less offset in N_{tot} and the PR4 measurement is slightly more precise than PR3's. Notably, however, PR4 in general prefers higher values of Y_{He} regardless of the value of N_{tot} . Comparing the two-dimensional posteriors that do and do not assume the prediction from BBN, for which Y_{He} increases with N_{tot} , suggests that PR4's preference for larger N_{tot} when assuming consistency with BBN is driven by its preference for larger values of Y_{He} . This comparison also suggests that PR3 data is modestly more consistent with SM predictions for Y_{He} . Moreover, the N_{tot} posteriors for PR4 and PR3 both center at 3 when marginalizing over Y_{He} . This suggests that the effects of changing Y_{He} better explain the differences between the two datasets than any effect deriving specifically from the radiation content.

To investigate the origin of PR4's preference for larger values of Y_{He} , Fig. 15 displays the residuals of CMB spectra for 1000 posterior samples for both PR4 and PR3 (i.e., those presented in Fig. 14 with N_{tot} , f_{fs} and Y_{He} free), each colored by its value of Y_{He} . These results indicate that PR4 prefers both excess damping in temperature at high ℓ and a higher polarization amplitude at $100 \leq \ell \leq 1000$ (driven by about half of the data in this interval skewing several standard deviations above the best-fit prediction). Both features can be better fit by increasing Y_{He} , deriving from the incurred slowing of recombination. Namely, with slower recombination the quadrupole has more time to radiate before last scattering,

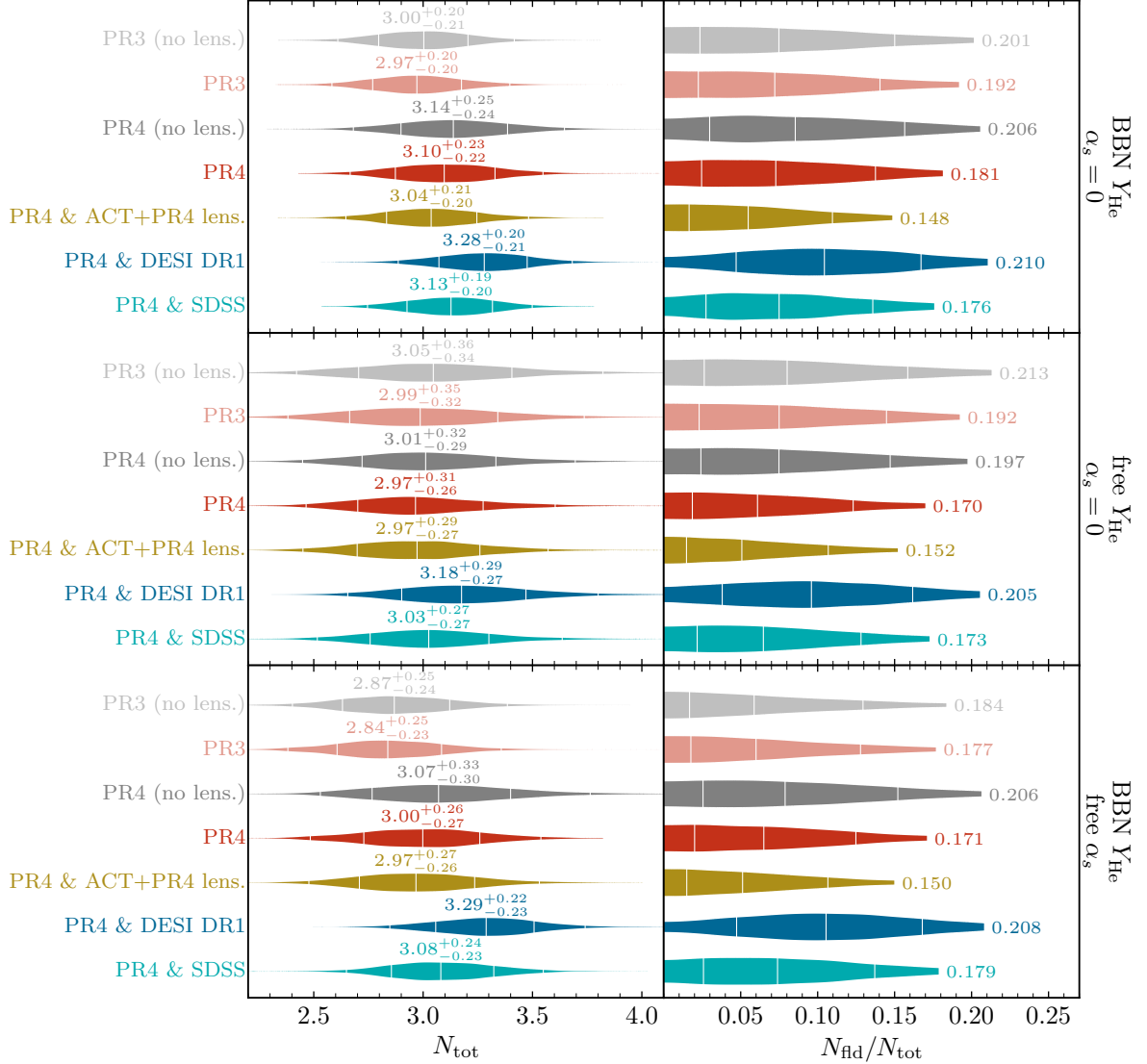


Figure 13. Posterior distributions for N_{tot} and $N_{\text{fid}}/N_{\text{tot}}$ for models with N_{tot} and f_{fs} free. Results are derived using *Planck* PR3 and PR4 CMB data, with or without lensing, and in combination with BAO data from DESI and SDSS or lensing data from ACT DR6 as labeled. The primordial helium yield Y_{He} is fixed to the BBN prediction in the top panels and independently varied in the middle panels. The bottom panels marginalize over the running of the spectral tilt α_s , again fixing Y_{He} to the BBN prediction. Posteriors on the left are labeled by their median and 1σ quantiles, with corresponding white lines indicating the median, 1σ , and 2σ contours. On the right, posteriors are truncated at the 95th percentile (whose value is also labeled); vertical white lines indicate the median and $\pm 1\sigma$ quantiles.

generating a larger amplitude of polarization [50, 51, 73]. A broader visibility function also increases the degree of so-called Landau damping on small scales [50, 74].

Figure 14 also displays results that vary all of N_{tot} , f_{fs} , and α_s . As noted in Section 2.1.2, the running of the spectral tilt can mimic the effect of small-scale damping by changing initial conditions rather than dynamics. Marginalization over the running slightly weakens constraints on N_{tot} with either PR3 or PR4 data. However, α_s cannot mimic the enhancement

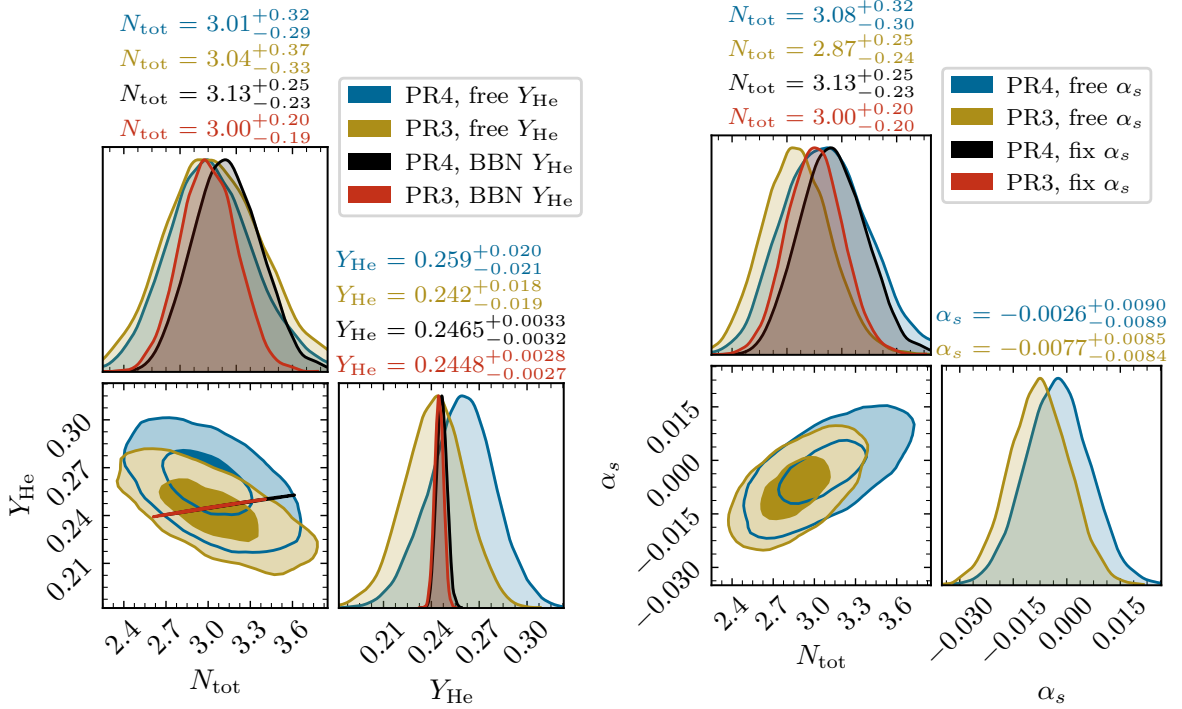


Figure 14. Posterior distributions for models where N_{tot} and f_{fs} both vary, comparing results using the *Planck* PR3 and PR4 temperature and polarization data (excluding lensing data). In the left figure, Y_{He} is either independently varied (blue and gold for PR4 and PR3, respectively) or fixed to the BBN prediction (black and red). The right figure compares results that also vary α_s (blue and gold) to those that fix it to zero (black and red), both with Y_{He} set to its BBN prediction. Diagonal panels depict kernel density estimates of one-dimensional posterior distributions normalized relative to their peak value to facilitate comparison. The median and corresponding $\pm 1\sigma$ uncertainties for each parameter are reported above the diagonal panels. The off-diagonal panels display the 1 and 2σ contours of the two-dimensional joint posterior density for pairs of parameters (i.e., the 39.3% and 86.5% mass levels).

of the polarization amplitude from increasing Y_{He} as preferred by PR4 data. PR3 favors negative running more so than PR4, as attributed to mild tensions between low and high multipoles in ΛCDM [1], correlating to a slightly lower radiation density. In contrast to results for ΛCDM parameters, PR4 yields slightly weaker constraints than PR3 on α_s (as well as on N_{tot} and Y_{He}), in curious contradiction to its greater data volume and multipole range. This finding may derive from the aforementioned internal inconsistencies in PR3 data [1] that may be mitigated in PR4, a possibility that warrants further investigation.

3.1.2 Role of CMB lensing data

As was true with the *Planck* PR3 data release [1, 26], incorporating PR4 lensing data does not qualitatively impact parameter inference for models that vary both N_{tot} and f_{fs} , as shown in Fig. 13. *Planck*'s CMB lensing data lack the precision to meaningfully break parameter degeneracies in the manner discussed in Section 2.4. ACT's DR6 lensing data also have little impact on the inference of N_{tot} , regardless of what additional parameters are varied (Y_{He} or α_s). However, ACT lensing data (in combination with PR4) do have a noticeable impact on the fraction of radiation that is fluidlike.

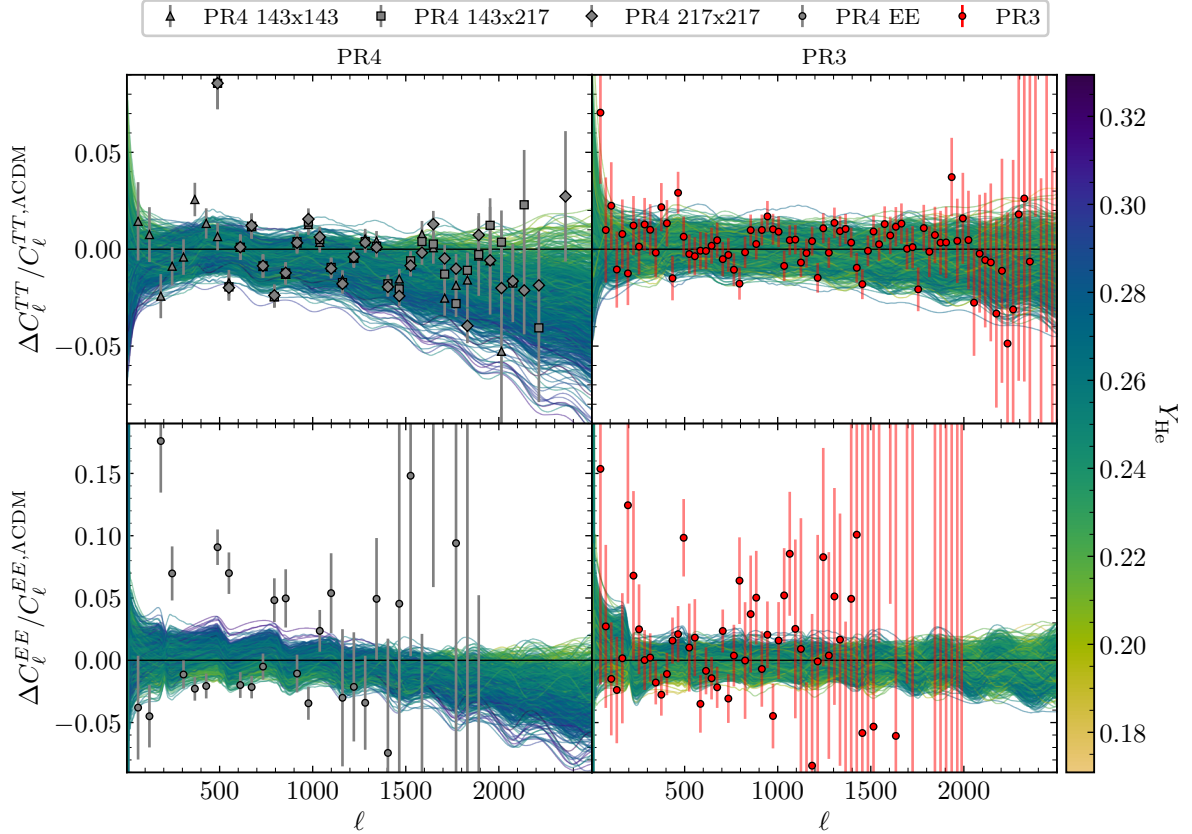


Figure 15. Residuals of the CMB temperature and polarization spectra relative to the Λ CDM best fit (derived from PR3 data) for samples from posteriors with N_{tot} , f_{fs} , and Y_{He} as free parameters. The left and right panels use PR4 and PR3 temperature and polarization data, respectively, both excluding lensing data. Curves are colored by each sample’s value of Y_{He} ; binned data are depicted as labeled in the legend (indicating the frequencies in GHz of the specific PR4 maps).

The increase in constraining power with ACT lensing data derives from effects of varying the free-streaming fraction—in particular, by better measuring A_s and breaking its degeneracy with f_{fs} (see Section 2.4).⁴ Figure 16 compares posteriors from PR4 that exclude and include lensing data from PR4 and from the combination of ACT DR6 and PR4. Decreasing the free-streaming fraction increases the amplitude of the CMB temperature and polarization spectra, requiring a reduced A_s to fit the data (Section 2.3). However, moving along the shift degeneracy exacerbates differences in the lensing potential (see Fig. 12). Therefore, the additional lensing information disfavors only the lower values of A_s allowed by the primary CMB. Since models with additional N_{fld} radiation prefer lower values of A_s , the addition of the PR4 + ACT DR6 lensing likelihood reduces the fraction of radiation that can be fluidlike, as is seen in the posteriors over f_{fs} and $N_{\text{fld}}/N_{\text{tot}}$ in Fig. 16. Upper limits on N_{tot} also decrease slightly, since the possibility of adding radiation in fluidlike form is more limited.

⁴Note that the impact of CMB lensing data depends sensitively on the inference of the optical depth from low- ℓ polarization data, which is required to determine A_s from $A_s = A_s e^{-2\tau_{\text{reio}}}$.

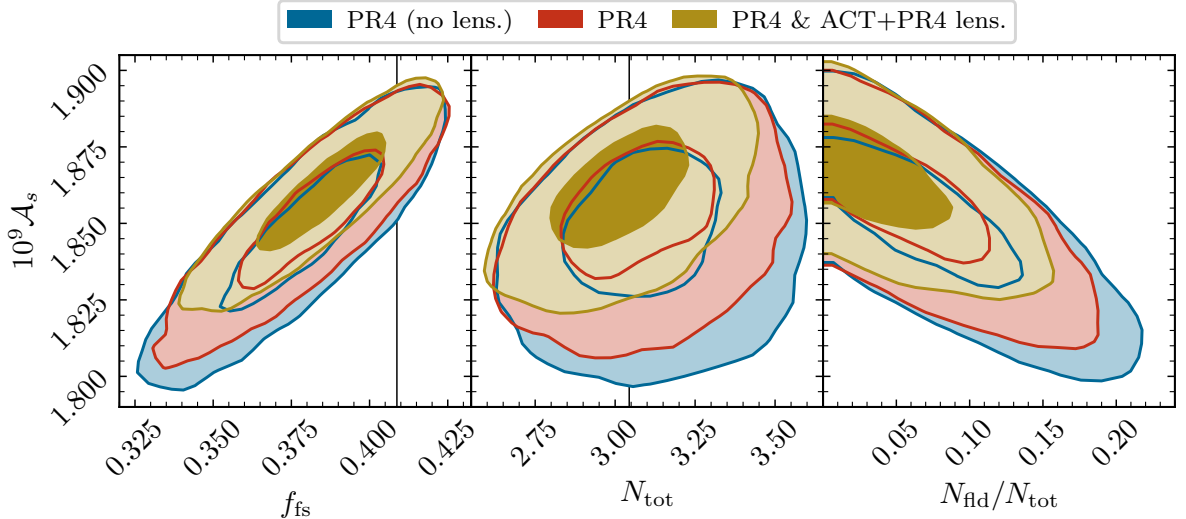


Figure 16. Joint posteriors over N_{tot} , $N_{\text{fid}}/N_{\text{tot}}$, and $\mathcal{A}_s = A_s e^{-2\tau_{\text{reio}}}$ for models varying both N_{tot} and f_{fs} , fixing Y_{He} to BBN predictions and using PR4 CMB data without lensing (blue), with PR4 lensing (red), and with PR4+ACT DR6 lensing (gold). The measurement of the amplitude of structure from CMB lensing data partly break the degeneracy between \mathcal{A}_s and f_{fs} , tightening upper limits on $N_{\text{fid}}/N_{\text{tot}}$; the marginal posteriors over N_{tot} are less affected. These findings also hold when α_s or Y_{He} freely vary.

3.1.3 Preference for additional radiation with BAO data

We now study the impact of low-redshift distance measurements from baryon acoustic oscillations. In models (like those we consider here) whose late-time expansion histories are well described by the flat Λ CDM model, low-redshift distance measurements only contribute meaningfully in models with some degree of geometric degeneracy in the distance to last scattering: within the standard six-parameter Λ CDM model, *Planck*'s measurements of θ_s and ω_{cb} indirectly constrain the late-time expansion history better than do direct measurements from BAO or supernovae distances. These data, however, are crucial in scenarios with geometric freedom in the CMB—for example, when taking the neutrino mass sum as a free parameter [75], in early recombination scenarios [51], or in models departing from flat Λ CDM at late times.

BAO distances are effectively parameterized by the matter fraction $\Omega_m = \omega_m/(\omega_m + \omega_\Lambda)$ (which encodes the redshift dependence, i.e., when the dark-energy era began) and $\omega_m r_d^2$ [75], where $\omega_m = \omega_b + \omega_c + \omega_\nu$ is the density in matter at late times⁵ and r_d the comoving sound horizon of the plasma at the time baryons decouple [76]. In dark radiation models, one would naively expect no such additional freedom when θ_s and a_{eq} are fixed, because then $\omega_\Lambda \propto \omega_{cb} \propto \omega_r$ [51, 75]. In this case, Ω_m is unchanged, and, because the sound horizon is inversely proportional to $\sqrt{\omega_r}$ at fixed a_{eq} , $\omega_m r_d^2 \approx \omega_{cb} r_d^2$ is unchanged as well. However, Fig. 2 shows that, due to the competing effect of changes to the pressure-supported matter fraction, posteriors from *Planck* do not precisely follow $\omega_{cb} \propto \omega_r$ —that is, the posteriors are driven by a compromise between fixing ω_{cb}/ω_r (which fixes the radiation-driving and early integrated Sachs-Wolfe effects) and ω_b/ω_{cb} . We now test the impact of BAO data in breaking

⁵The distinction between ω_{cb} and ω_m is irrelevant because our analyses fix the neutrino mass sum and therefore fix ω_m as a function of ω_{cb} .

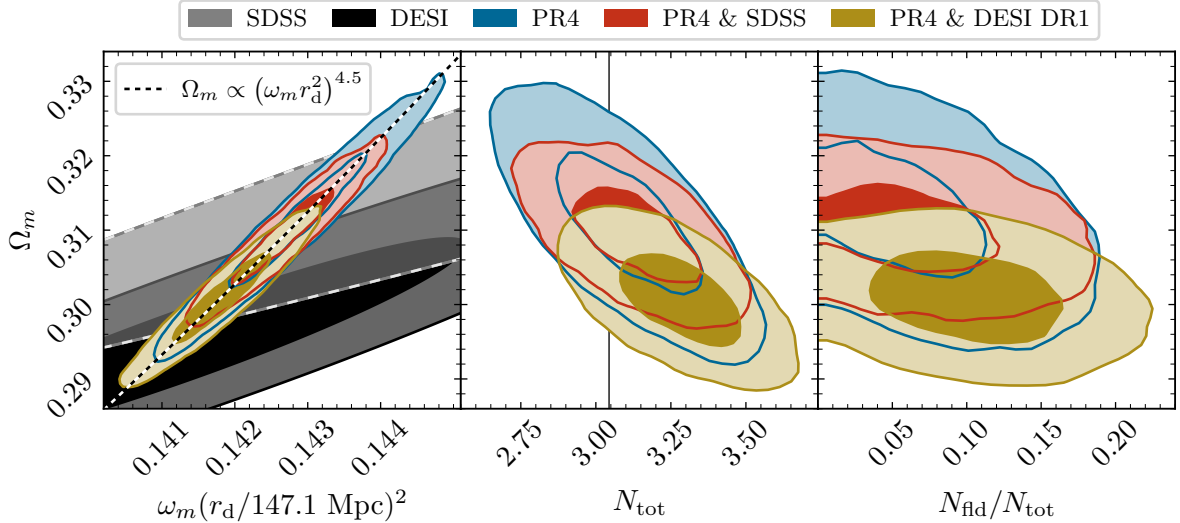


Figure 17. Joint posteriors over $\omega_m r_d^2$, N_{tot} , $N_{\text{fid}}/N_{\text{tot}}$, and Ω_m for models varying N_{tot} and f_{fs} , using dataset combinations labeled in the legend. The posteriors deriving from SDSS (grey, dashed) or DESI (black) alone display constraints for the flat Λ CDM model (following Ref. [75]), and their overlap with the PR4 CMB-only posterior (blue) determines the extent of the joint posteriors (red and gold). Note that only one end of SDSS’s 2σ region is visible within the axes limits; since we only use a subset of eBOSS tracers, the joint posterior is centered at larger Ω_m and $\omega_m r_d^2$ than depicted.

the resulting additional geometric freedom.

Interestingly, Fig. 13 shows that DESI data push posteriors toward greater values of N_{tot} across all model extensions. DESI BAO data prefer a lower matter fraction (at any given $\omega_m r_d^2$) compared to *Planck* data alone, as evident in the posteriors in Fig. 17. The CMB’s geometric degeneracy is clear in the joint posterior over Ω_m and $\omega_m r_d^2$ in Fig. 17; analytically, fixing θ_s in flat Λ CDM cosmologies approximately requires [75]⁶

$$\Omega_m|_{\theta_s} \propto (\omega_m r_d^2)^5. \quad (3.1)$$

Because ω_m increases sublinearly with ω_r (see Fig. 2), the matter fraction can be reduced (as preferred by DESI) when increasing ω_r while still satisfying the degeneracy direction in Eq. (3.1). BAO data from SDSS do not drive the same preference for larger ω_r , as also evident in Fig. 13, because the SDSS data prefer a larger matter fraction at any $\omega_m r_d^2$ than DESI, closer to those PR4 infers in Λ CDM. Note that Ref. [75] showed that DESI’s preference for lower Ω_m than SDSS derives entirely from the two measurements that are most in tension with those from SDSS.

To maintain concordance with CMB data, the preference for additional radiation in constraints that include the DESI DR1 BAO data is mostly accomplished through the addition of fluidlike radiation. Since the CMB prefers f_{fs} close to the Λ CDM value and N_{fid} affects f_{fs} less dramatically than additional free-streaming radiation [per Eq. (2.16)] the posteriors for $N_{\text{fid}}/N_{\text{tot}}$ shift to higher values (Fig. 13) across all model extensions when including DESI data.

⁶Note that a numerical fit derived from the PR4-only posteriors yields $\Omega_m \propto (\omega_m r_d^2)^{4.5}$, as displayed in dashed black in Fig. 17. The deviation in exponent from that in Eq. (3.1) is due to correlations of θ_s with ω_b and ω_c as well as the free-streaming fraction f_{fs} , none of which are accounted for in the approximations that yield Eq. (3.1).

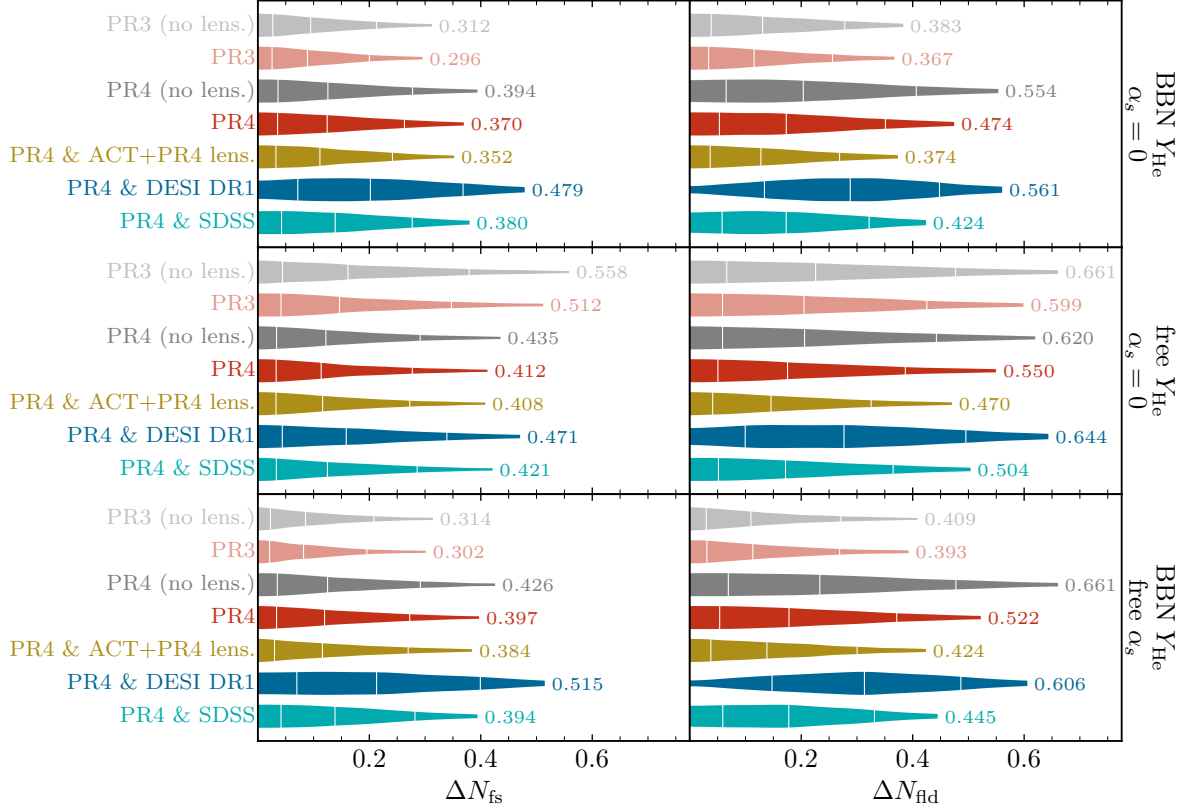


Figure 18. Marginal posterior distributions over ΔN_{fs} and ΔN_{fld} for models adding either free-streaming or fluidlike dark radiation. Results are presented as in Fig. 13.

3.2 Constraints on interacting and noninteracting dark radiation

We now turn to models that strictly allow radiation in addition to the contributions from SM neutrinos of $N_{\text{tot}} = N_{\text{fs}} = 3.044$, parametrized by ΔN_{fs} and ΔN_{fld} . We interpret these results as special cases of Section 3.1, which allowed for arbitrary amounts of free-streaming and fluidlike radiation, as varying ΔN_{fs} or ΔN_{fld} prescribes a specific relationship between the total density ω_r and the free-streaming fraction f_{fs} . We continue to examine the impact of all three model extensions considered above: Y_{He} fixed to the BBN prediction, Y_{He} allowed to freely vary, and α_s allowed to vary. The marginal posterior distributions for these models are reported in Fig. 18. Consistent with our findings for models with N_{tot} and f_{fs} both free, PR4 allows for slightly more radiation than PR3 across all model extensions, deriving from differences in the polarization amplitude that drive a preference for higher helium yield (see Fig. 15).

Like the case with N_{tot} and f_{fs} both free, the combination of PR4 and ACT DR6 lensing data has a substantially greater impact on upper limits than the PR4 lensing data alone. In particular, lensing has the greatest impact on ΔN_{fld} . As mentioned in Section 2.3, additional fluidlike radiation decreases the free-streaming fraction [per Eq. (2.16)], which boosts the amplitude of both the temperature and polarization power spectra. In turn, lower values of \mathcal{A}_s are required to fit the data. However, lensing data drive a preference for higher values of \mathcal{A}_s (Fig. 16), further restricting ΔN_{fld} . Even when marginalizing over Y_{He} and α_s , the addition of ACT lensing data significantly improves upon PR4 in limits on ΔN_{fld} . In contrast,

constraints from PR3 alone are stronger than PR4 and ACT DR6 constraints when Y_{He} is consistently set to the BBN predictions, driven by PR3 data’s independent preference for a lower radiation density (see Section 3.1.1).

The preference for additional radiation when including DESI BAO data persists in models with $\Delta N_{\text{fs/fld}}$, regardless of variations in Y_{He} and α_s . BAO data from SDSS, on the other hand, have little effect because its geometric preferences are more consistent with *Planck*’s. DESI data drive a more substantial preference for ΔN_{fld} than ΔN_{fs} since the former’s effects in the CMB are less distinctive (see Section 2.3). This preference for a greater radiation density (and therefore a smaller sound horizon) in turn pushes H_0 to larger values $69.8_{-1.1}^{+1.2}$ km/s/Mpc (see Appendix B) as reported in Ref. [77]. Models with fluidlike dark radiation that take the BBN predictions for Y_{He} have a median value of H_0 value 2.1σ away from that from SH0ES [78], while in the free-streaming case the tension is 2.7σ . Allowing Y_{He} and α_s to vary does not significantly improve the agreement of H_0 to the local measurement.

3.3 Forecasts for CMB-S4

The planned CMB-S4 experiment is expected to improve constraints on N_{fs} by almost an order of magnitude. In this section, we forecast measurements for CMB-S4 in the models studied above, using noise curves for the latest configuration [39]. We implement these forecasts with the `mock_cmb_likelihood` from `MontePython` [79, 80]. We use the mean of the posteriors for Λ CDM parameters from the *Planck* PR4 dataset for the fiducial cosmology (see the first column of Table 3). We also take a Gaussian prior over τ_{reio} with mean 0.0577 and standard deviation 0.0062 as provided by *Planck* PR4 data, as CMB-S4 will not have access to the large scale modes that directly constrain reionization.

We implement a joint likelihood including lensed temperature and polarization as well as reconstructed lensing spectra. We find that, for the class of models considered here, unlensed spectra give nearly identical results as lensed spectra, with the only difference being that unlensed spectra yield slightly more precise measurements of θ_s .⁷ These findings are consistent with prior Fisher forecasts for N_{fs} [81], which further only a small improvement from delensing the primary anisotropies. Our use of lensed spectra is thus more conservative than using spectra that are delensed or fully unlensed (i.e., the idealized limit of perfect delensing). We also neglect the non-Gaussian contributions to the covariance induced by lensing, which Ref. [81] found had little effect on N_{fs} forecasts. Although these non-Gaussian contributions have been shown to lead to overly optimistic constraints on A_s , we find that our forecasts are unaffected, despite the interesting interplay between A_s and fluidlike radiation (Section 2.3.1). We leave a proper treatment of delensing and covariance in CMB-S4 forecasts to future work.

CMB-S4’s design sensitivity requires accurate modeling of nonlinear structure growth. At $\ell = 1500$ in the lensing potential spectra, the linear and nonlinear power spectra differ by nearly 20%, which CMB-S4 will easily differentiate between. To model these nonlinearities, we use `HMCode-2016` [82] with `nonlinear_min_k_max` set to 5 Mpc^{-1} .⁸ Although `HMCode` is calibrated to simulations that do not include additional light relics, we find that it gives similar results to `CLASS_PT` [83], which consistently treats differences to matter perturbations

⁷Delensing the primary anisotropies effectively removes the peak smearing caused by lensing, providing more precise peak location information and improving bounds on θ_s [81]. Delensing and a more careful modeling of covariance are more important for physics related to late-time structure, such as massive neutrinos (which suppress structure growth).

⁸We find that increasing `nonlinear_min_k_max` to larger values does not substantially change the lensing potential spectra relative to CMB-S4’s sensitivity.

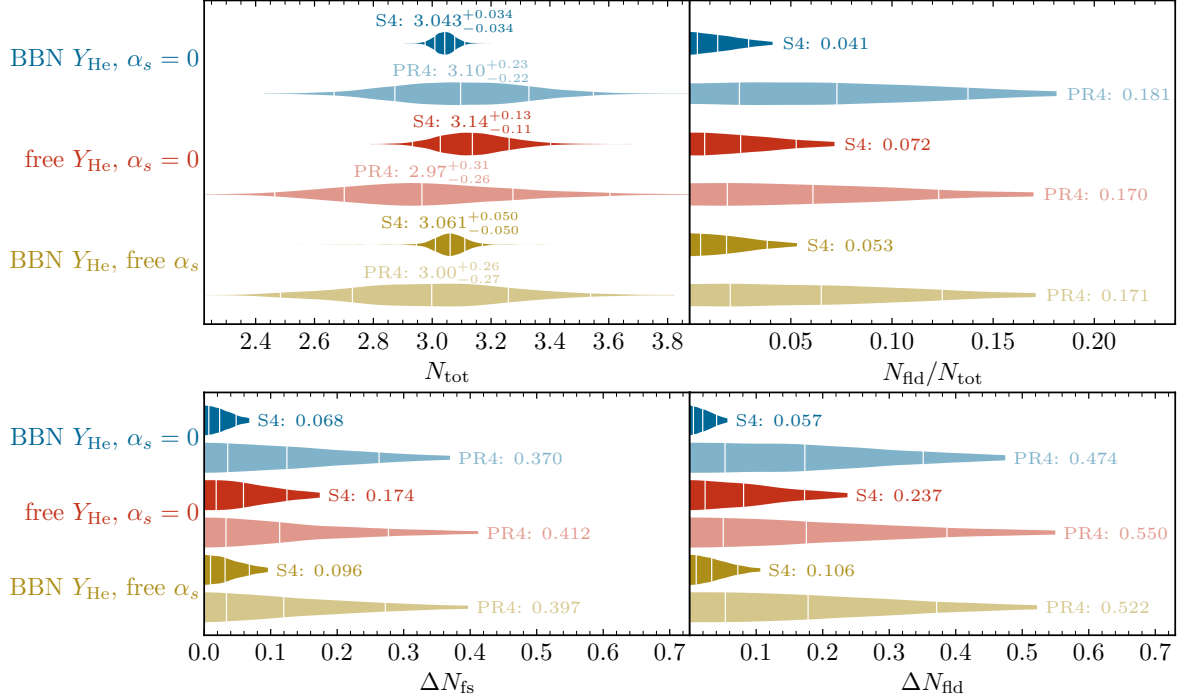


Figure 19. Forecasted constraints from CMB-S4 compared with current ones from the *Planck* PR4 dataset for models with N_{tot} and f_{fs} free (top) as well as models with additional free-streaming or fluidlike radiation (bottom). Both cases included lensing reconstruction data. Results are shown for models with Y_{He} set to its BBN prediction, Y_{He} freely varying, and α_s freely varying as labeled.

due to the additional dark radiation within standard perturbation theory at one loop. Since the differences between the two nonlinear codes is only at the percent-level, we opt to use *HMCode* for simplicity.

We present forecasts for models with N_{tot} and f_{fs} free, as well as models individually varying ΔN_{fld} and ΔN_{fs} , in Fig. 19. When Y_{He} is fixed to its BBN prediction, we observe a factor of seven improvement in sensitivity in N_{tot} between the *Planck* PR4 dataset combination and CMB-S4, with the 1σ intervals improving from $\sigma(N_{\text{tot}}) = 0.23$ to $\sigma(N_{\text{tot}}) = 0.034$. The cases with Y_{He} free show only a factor of three improvement in sensitivity. However, the 1σ interval for Y_{He} also improves by a factor of three; we forecast a measurement $\sigma(Y_{\text{He}}) \sim 0.008$ from CMB data alone with CMB-S4, independent of BBN [see Fig. 21 in Appendix B.] In models with α_s free, CMB-S4 yields a similar factor of six improvement for N_{tot} and a factor of 2.2 for α_s , improving from $\sigma(\alpha_s) = 8.4 \times 10^{-3}$ with PR4 data to $\sigma(\alpha_s) = 3.8 \times 10^{-3}$ with CMB-S4.

For models with additional radiation on top of the minimum ΛCDM prediction for N_{fs} , CMB-S4 will improve sensitivity to both free-streaming and fluidlike radiation by nearly a factor of five when taking BBN predictions for Y_{He} . The 95% upper limit on additional free-streaming radiation improves from $\Delta N_{\text{fs}} \leq 0.37$ to $\Delta N_{\text{fs}} \leq 0.068$, while that for fluidlike radiation improves from $\Delta N_{\text{fld}} \leq 0.47$ to $\Delta N_{\text{fld}} \leq 0.057$. Figure 19 displays comparable improvements in sensitivity when Y_{He} and α_s are free.

4 Conclusions

In this paper, we studied the cosmological signatures of the radiation content of the early Universe—in particular, considering scenarios beyond the predictions for SM neutrinos that feature light degrees of freedom that are strongly self-interacting, collisionless, or both in some proportion. In Section 2, we reviewed the physical origin of parameter degeneracies in the CMB anisotropy spectra that arise in such scenarios, phrasing the relevant effects in terms of the total radiation density ω_r and the fraction f_{fs} thereof that freely streams (as SM neutrino do after weak decoupling) in order to disentangle which parameters are affected by different physical effects. A clear understanding of the degeneracies that result in particular observables provides physical insight into the status of light relics with current observations and clarifies how combining multiple probes breaks these degeneracies.

Beyond the well-established degeneracy between ω_r and the helium yield Y_{He} , we identified a partial degeneracy between ω_r , n_s , and ω_b , which we coin a “tilt” degeneracy (Section 2.1.1) due to its origin in the scale dependence of the CMB temperature and polarization spectra. We also explored how varying the running of the tilt, α_s , can mitigate the impact of small-scale damping induced by additional radiation. Then we reviewed the fact that, when isolating the background-level effects of extra radiation by fixing ω_r , the remaining physical effects encoded by the free-streaming fraction f_{fs} are a phase and amplitude shift in the acoustic peaks. As a result, f_{fs} is strongly anticorrelated with θ_s and correlated with A_s (as well as n_s and ω_b , to a lesser extent) via the “shift” degeneracy (Section 2.2.1). Neither of the degeneracies with A_s and θ_s are exact; changes to f_{fs} only predict a constant amplitude shift at small scales, and an additive phase shift cannot be exactly reproduced by scaling θ_s .

Having established the relevant physical effects for the general case featuring arbitrary amounts of fluidlike and free-streaming radiation, we turned to specific new-physics scenarios that introduce new light relics (on top of SM neutrinos) that either are or are not strongly self-interacting. When interpreted in the ω_r - f_{fs} parameter space, the two cases differ in whether the free-streaming fraction increases or decreases with the total radiation density (see Eq. (2.16)). We detailed how additional free-streaming and fluidlike radiation consequently affect the amplitude of the first peak of the CMB primary power spectrum differently. For models featuring fluidlike radiation, the effects of changing the fraction of pressure-supported matter and the free-streaming fraction conspire on small scales to hide oscillatory effects: the former shifts the zero point of the acoustic oscillations, cancelling some of the phase shift incurred by the latter. The two effects, however, exacerbate the scale-independent boost in amplitude on small scales but act in tandem to largely preserve the amplitude of the first acoustic peak. The first peak thus plays a key role in determining A_s and therefore constraining ΔN_{fld} , as discussed in Section 2.3.1. In contrast, the shift of the acoustic peaks is more severe with additional free-streaming radiation, for which reason constraints on ΔN_{fs} are typically stronger than those on ΔN_{fld} .

In Section 3, we updated constraints on models with additional light relics using the latest *Planck*, ACT lensing, and DESI data releases, as tabulated in Figs. 13 and 18. We also studied how constraints degrade upon freeing the primordial helium fraction Y_{He} or the running of the primordial spectral tilt, α_s . *Planck* PR4 CMB data alone do not show a preference for additional fluidlike or free-streaming radiation, with the Λ CDM prediction for N_{tot} being within about 1σ of the posterior medians across all model extensions and dataset combinations (see Fig. 13). In general, the data allow for slightly more fluidlike radiation than free-streaming radiation, due to the aforementioned, differing interplay between the

composition of the matter and radiation content.

Interestingly, we showed in Fig. 14 that the PR4 reanalysis of the *Planck* data prefers a larger value for the helium yield, whose origin Fig. 15 identified as a higher preferred polarization amplitude in PR4 data at $\ell \lesssim 1000$ (both compared to Λ CDM predictions and to PR3 data). Increasing Y_{He} prolongs recombination, generating a larger polarization signal at last scattering, and increases damping, which PR4 temperature data also slightly prefer. When enforcing consistency with BBN predictions, this preference for a larger helium yield propagates to a preference for greater N_{tot} for both fluidlike and free-streaming radiation. This same feature would likely drive a preference for other Λ CDM extensions that modify the shape of the visibility function, such as a time-varying fine-structure constant [51]. However, the data driving this trend are not especially well fit by the model, even with the additional freedom of N_{tot} and Y_{He} : about half of the binned spectra in this range skew multiple standard deviations beyond the support of the posteriors (as projected into the data space), while the others agree more closely. The robustness of these features in PR4 data (and any conclusions depending upon them) merit further scrutiny, especially given their absence in PR3 data.

We also found that recent CMB lensing data from ACT DR6 (combined with *Planck* PR4) tighten upper limits on models with additional fluidlike radiation, deriving from their preference for a lensing amplitude in excess of Λ CDM predictions. Since lower free-streaming fractions require a smaller amplitude A_s to fit the temperature and polarization data, additional fluidlike radiation is more strongly restricted by the addition of lensing data. Regardless of the dataset combination or model extension, we find that the fraction of the radiation density (excluding photons) that is fluidlike is limited to $N_{\text{fld}}/N_{\text{tot}} \leq 21\%$ at the 95% level, as seen in Figs. 13 and 18. This result holds even when Y_{He} and α_s are free parameters.

Including BAO data from DESI yields a slight preference for extra radiation, deriving from its interplay with the CMB’s geometric degeneracy (see Fig. 17). Increasing the radiation density shifts and extends *Planck*’s preferences along the geometric degeneracy toward the parameter space preferred by DESI; this phenomenon is more effective under additional fluidlike radiation, again because its effects that modulate the acoustic peaks partially cancel. Using BAO measurements from prior surveys does not yield a similar preference, as DESI’s prefer smaller matter fractions Ω_m than other observations. This preference for additional radiation with DESI BAO data lead the CMB to infer larger Hubble constants $H_0 = 69.8^{+1.2}_{-1.1}$ km/s/Mpc, as observed in [77].

In Section 2.4, we explored how large-scale-structure observations can break both the “tilt” degeneracy as well as the degeneracy between N_{tot} and Y_{He} . Full-shape data from spectroscopic galaxy surveys stand to significantly improve inferences of N_{tot} and Y_{He} [84], a possibility worthy of future investigation (for instance, with new measurements from DESI [85]). In addition, measurements of the light element abundances constrain the radiation density at higher temperatures than does the CMB, which can improve measurements on N_{tot} [86–88] or probe its possible evolution between nucleosynthesis and recombination [89–91]. The CMB, however, is sensitive to not just the total radiation density but also its interactions.

In general, the partial degeneracies at play in the CMB can be significantly abated by higher resolution observations from ongoing and future CMB experiments. Recent data from the Atacama Cosmology Telescope [92] and the South Pole Telescope [93], which observe deeper into the damping tail and offer improved precision in polarization even on moderate scales, should improve meaningfully upon *Planck*. Our discussion of fluidlike radiation—namely, the importance of the first acoustic peaks emphasized in Section 2.3—may shed light on a reported preference for strongly interacting neutrinos in ACT DR4 data [56]: the

strongest preferences derive from results that exclude CMB data other than ACT’s high- ℓ observations or that include data from the Wilkinson Microwave Anisotropy Probe [94, 95] rather than *Planck*. Given that DESI’s DR1 BAO data are also best accommodated (in combination with *Planck*) by extra fluidlike radiation, these scenarios warrant further study with future data.

Finally, we forecasted the CMB-S4 experiments’s sensitivity to additional light relic degrees of freedom (see Fig. 19), using its current planned configuration. These observations will dramatically diminish the degeneracies at play in current data, improving sensitivity to both the existence of light relics as well as the nature of their interactions. In models where the total radiation and the free-streaming fraction are both allowed to vary, CMB-S4 can reach a sensitivity of $\sigma(N_{\text{tot}}) \sim 0.03$ and a limit on the fluidlike fraction of new radiation of $N_{\text{fld}}/N_{\text{tot}} \lesssim 4\%$ (at the 95% level). These future measurements—roughly five times better than present ones—promise an era of percent-level constraints on not just the existence of new light relics but also their fundamental nature.

Acknowledgments

We thank Francis-Yan Cyr-Racine, Benjamin Wallisch, Srinivasan Raghunathan, Kimberly Boddy, Cynthia Trendafilova, Nikita A. Zemlevskiy, Jacob W. Crawford, Ella C. Henry, Caio Bastos de Senna Nascimento, Charuhas Shiveshwarker, John Franklin Crenshaw, and Roland C. Farrell for advice and helpful discussions. We also thank Steven Gratton and Erik Rosenberg for providing binned `CamSpec` spectra.

MMS and ML are supported by the Department of Energy grants DE-SC0023183 and DE-SC0011637. TB was supported by ICSC – Centro Nazionale di Ricerca in High Performance Computing, Big Data and Quantum Computing, funded by European Union – NextGenerationEU. Research at Perimeter Institute is supported in part by the Government of Canada through the Department of Innovation, Science and Economic Development and by the Province of Ontario through the Ministry of Colleges and Universities. This work was enabled, in part, by the use of advanced computational, storage, and networking infrastructure provided by the Hyak supercomputer system at the University of Washington, which was supported by the UW Student Technology Fee [96]. This work made use of the software packages `corner.py` [97], `NumPy` [98], `SciPy` [99], `matplotlib` [100], `xarray` [101].

A Constraining power of different multipole ranges

Section 2.3.1 demonstrates the importance of the height of the first peak plays in constraining N_{fld} . To test the impact of this effect on parameter inference, we constrain ΔN_{fs} and ΔN_{fld} using mock CMB temperature and polarization data divided into two multipole ranges: $1000 \leq \ell \leq 2500$, which excludes the first three peaks but captures the damping tail, and $\ell \leq 2500$, which includes the full spectra. We generate a mock CMB dataset with *Planck* PR3-like noise and use the `fake_planck_bluebook` likelihood in `MontePython` version 3.6 interfaced with the Boltzmann solver `CLASS` 3.2.3 [42, 79, 80]. The fiducial cosmology takes $\omega_b = 0.02236$, $\omega_c = 0.1202$, $100\theta_s = 1.0409$, $\ln(10^{10} A_s) = 3.045$, $n_s = 0.965$, $\tau_{\text{reio}} = 0.0544$, and $N_{\text{fs}} = 3.046$ with Y_{He} fixed to its BBN prediction. We employ the Metropolis-Hastings algorithm in `MontePython` for sampling and a Gelman-Rubin convergence criterion of $R - 1 \lesssim 0.01$, leading to effective sample sizes of at least 20,000.

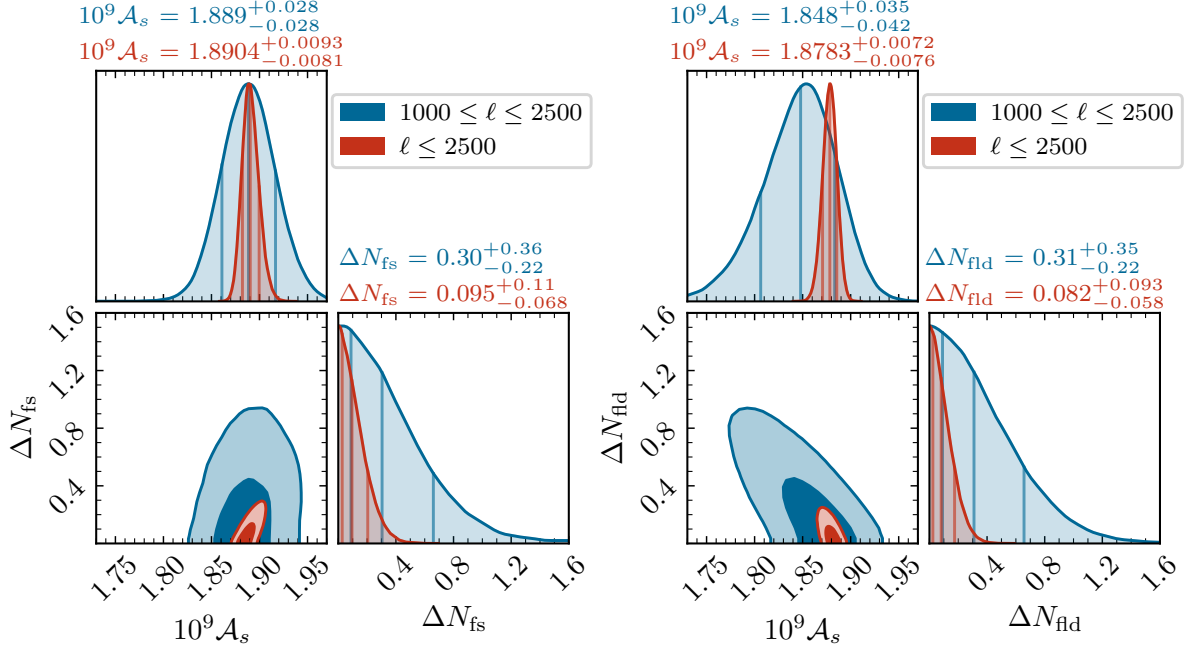


Figure 20. Posterior distribution for $\mathcal{A}_s e^{-2\tau_{\text{reio}}}$ and additional radiation (ΔN_{fs} , left, and ΔN_{fld} , right) for a mock-*Planck* likelihood over $\ell \leq 2500$ (red) and restricted to $1000 \leq \ell \leq 2500$ (blue). Results are presented as in Fig. 14.

In Fig. 20, we plot the posterior distributions for ΔN_{fs} and ΔN_{fld} (each varied independently) along with $\mathcal{A}_s = \mathcal{A}_s e^{-2\tau_{\text{reio}}}$, since this combination of parameters controls the overall amplitude of the spectra. With additional free-streaming radiation, posteriors for $1000 \leq \ell \leq 2500$ and for the full multipole range are centered on essentially the same value of \mathcal{A}_s , as they show little degeneracy between \mathcal{A}_s and ΔN_{fs} . Contrast this result with the case with additional fluidlike radiation, where the medians are substantially offset from each other due to a clear degeneracy within high- ℓ data; the posterior over \mathcal{A}_s for the high- ℓ subset is also substantially broader under additional fluidlike radiation.

Evidently, the first peaks play much more of a role in breaking degeneracies with \mathcal{A}_s in models with additional fluidlike radiation, as anticipated from Section 2.3.1 based on the differing interplay between changes to the pressure-supported matter fraction and the free-streaming fraction. Notably, the posteriors over $\Delta N_{\text{fs/fld}}$ are extremely similar when using only high- ℓ data, while upper limits from the full multipole range are slightly tighter on ΔN_{fld} —namely, $\Delta N_{\text{fld}} < 0.25$ and $\Delta N_{\text{fs}} < 0.29$ at the 95% level. This comparison suggests that the impacts of the free-streaming fraction (Section 2.2) are only relevant insofar as they mediate the spectra at low and high multipole.

B Supplementary results

In this appendix, we provide constraints on Λ CDM, models with additional free-streaming or fluidlike radiation, and models where N_{tot} and f_{fs} are allowed to vary. Figure 21 depicts the marginalized posteriors over Y_{He} and α_s for models where they vary for all dataset combinations considered in this work. Tables 2 to 5 provide constraints on the Λ CDM parameters, N_{tot} , f_{fs} , and the fraction of radiation (outside the photons) that is fluidlike, $N_{\text{fld}}/N_{\text{tot}}$, as well as the

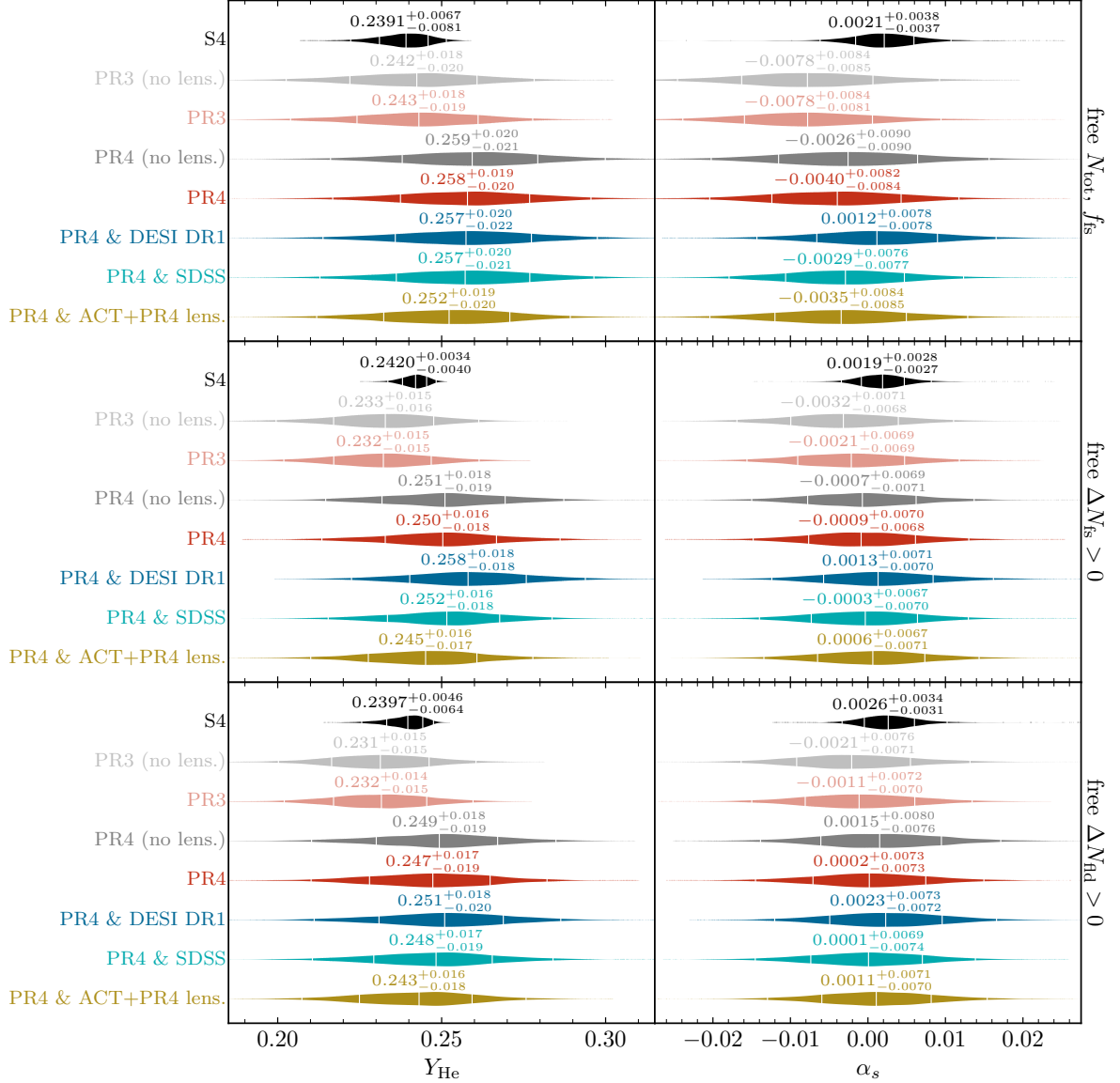


Figure 21. Marginal posterior distributions over Y_{He} and α_s in models where they freely vary. The S4 posteriors correspond to forecasts assuming the fiducial model detailed in Section 3.3 (see Fig. 19), while all others derive from current data (see Figs. 13 and 18). Note that the DESI and SDSS dataset combinations include PR4 lensing data. Results are presented as in Fig. 13.

derived parameters H_0 , r_d , Ω_m , and the amplitude of matter fluctuations, σ_8 . Table 2 reports results using only the *Planck* PR4 temperature and polarization data, while Table 3 includes PR4 lensing data, Table 4 also includes ACT DR6 lensing data, and Table 5 also includes DESI DR1 BAO data. Note that Y_{He} is fixed to the BBN prediction in these results.

References

- [1] PLANCK collaboration, *Planck 2018 results. VI. Cosmological parameters*, *Astron. Astrophys.* **641** (2020) A6 [1807.06209].

	Λ CDM	ΔN_{fs}	ΔN_{fld}	$N_{\text{tot}}, f_{\text{fs}}$
$100\theta_s$	$1.04175^{+0.00025}_{-0.00024}$	$1.04144^{+0.00031}_{-0.00035}$	$1.04201^{+0.00032}_{-0.0003}$	$1.04251^{+0.00072}_{-0.00066}$
ω_b	$0.02217^{+0.00014}_{-0.00014}$	$0.02227^{+0.00016}_{-0.00015}$	$0.02239^{+0.00022}_{-0.00019}$	$0.02233^{+0.00024}_{-0.00023}$
ω_c	$0.1196^{+0.0012}_{-0.0012}$	$0.1216^{+0.0022}_{-0.0018}$	$0.1226^{+0.0028}_{-0.0022}$	$0.1207^{+0.0037}_{-0.0036}$
$\ln(10^{10}A_s)$	$3.046^{+0.013}_{-0.013}$	$3.052^{+0.014}_{-0.014}$	$3.041^{+0.014}_{-0.014}$	$3.031^{+0.017}_{-0.018}$
n_s	$0.963^{+0.0043}_{-0.0042}$	$0.9679^{+0.006}_{-0.0052}$	$0.966^{+0.0047}_{-0.0046}$	$0.9602^{+0.0082}_{-0.0081}$
τ_{reio}	$0.0573^{+0.0062}_{-0.006}$	$0.0578^{+0.0063}_{-0.0061}$	$0.0581^{+0.0063}_{-0.0061}$	$0.0579^{+0.0063}_{-0.0061}$
ΔN_{tot}	—	< 0.39	< 0.55	$0.09^{+0.25}_{-0.23}$
f_{fs}	—	—	—	$0.378^{+0.024}_{-0.026}$
$N_{\text{fld}}/N_{\text{tot}}$	—	—	< 0.15	< 0.20
H_0 [km/s/Mpc]	$67.26^{+0.55}_{-0.53}$	$68.2^{+1.1}_{-0.8}$	$69.0^{+1.7}_{-1.2}$	$68.3^{+1.9}_{-1.7}$
r_d [Mpc]	$147.43^{+0.28}_{-0.27}$	$146.2^{+0.9}_{-1.4}$	$145.5^{+1.3}_{-1.8}$	$146.5^{+2.3}_{-2.3}$
Ω_m	$0.3148^{+0.0074}_{-0.0076}$	$0.3104^{+0.0077}_{-0.0079}$	$0.305^{+0.009}_{-0.01}$	$0.308^{+0.011}_{-0.011}$
σ_8	$0.8102^{+0.0064}_{-0.0064}$	$0.8158^{+0.008}_{-0.0073}$	$0.8121^{+0.0066}_{-0.0065}$	$0.805^{+0.011}_{-0.011}$

Table 2. Constraints on the extensions to Λ CDM considered in this work using the *Planck* PR4 TT, TE, and EE likelihoods (with no lensing included), with Y_{He} fixed to the BBN prediction. We present the median and $\pm 1\sigma$ quantiles for most parameters and 95% upper limits for $N_{\text{fld}}/N_{\text{tot}}$ and $\Delta N_{\text{fs}/\text{fld}}$. In all cases, $\Delta N_{\text{tot}} = N_{\text{tot}} - 3.044$ (whether from free-streaming radiation, fluidlike radiation, or both).

- [2] M.S. Turner, *Thermal Production of Not SO Invisible Axions in the Early Universe*, *Phys. Rev. Lett.* **59** (1987) 2489.
- [3] D. Baumann, D. Green and B. Wallisch, *New Target for Cosmic Axion Searches*, *Phys. Rev. Lett.* **117** (2016) 171301 [[1604.08614](#)].
- [4] M. Millea, L. Knox and B. Fields, *New Bounds for Axions and Axion-Like Particles with keV-GeV Masses*, *Phys. Rev. D* **92** (2015) 023010 [[1501.04097](#)].
- [5] K. Abazajian, G.M. Fuller and M. Patel, *Sterile neutrino hot, warm, and cold dark matter*, *Phys. Rev. D* **64** (2001) 023501 [[astro-ph/0101524](#)].
- [6] S. Weinberg, *Goldstone Bosons as Fractional Cosmic Neutrinos*, *Phys. Rev. Lett.* **110** (2013) 241301 [[1305.1971](#)].
- [7] Z. Chacko, Y. Cui, S. Hong and T. Okui, *Hidden dark matter sector, dark radiation, and the CMB*, *Phys. Rev. D* **92** (2015) 055033 [[1505.04192](#)].
- [8] M.A. Buen-Abad, G. Marques-Tavares and M. Schmaltz, *Non-Abelian dark matter and dark radiation*, *Phys. Rev. D* **92** (2015) 023531 [[1505.03542](#)].
- [9] A. Berlin and N. Blinov, *Thermal Dark Matter Below an MeV*, *Phys. Rev. Lett.* **120** (2018) 021801 [[1706.07046](#)].
- [10] C. Dvorkin et al., *The Physics of Light Relics*, in *Snowmass 2021*, 3, 2022 [[2203.07943](#)].

	Λ CDM	ΔN_{fs}	ΔN_{fld}	$N_{\text{tot}}, f_{\text{fs}}$
$100 \theta_s$	$1.04175^{+0.00024}_{-0.00024}$	$1.04146^{+0.00031}_{-0.00035}$	$1.04196^{+0.0003}_{-0.00029}$	$1.04243^{+0.00066}_{-0.00061}$
ω_b	$0.02217^{+0.00014}_{-0.00014}$	$0.02227^{+0.00015}_{-0.00015}$	$0.02235^{+0.0002}_{-0.00017}$	$0.02228^{+0.00022}_{-0.00021}$
ω_c	$0.1196^{+0.001}_{-0.001}$	$0.1215^{+0.0021}_{-0.0017}$	$0.1223^{+0.0026}_{-0.002}$	$0.1206^{+0.0034}_{-0.0035}$
$\ln(10^{10} A_s)$	$3.047^{+0.012}_{-0.012}$	$3.053^{+0.013}_{-0.013}$	$3.044^{+0.012}_{-0.012}$	$3.035^{+0.016}_{-0.016}$
n_s	$0.963^{+0.004}_{-0.0039}$	$0.9675^{+0.0057}_{-0.005}$	$0.965^{+0.0042}_{-0.0042}$	$0.9592^{+0.008}_{-0.0079}$
τ_{reio}	$0.0577^{+0.0062}_{-0.0059}$	$0.0582^{+0.006}_{-0.0059}$	$0.0589^{+0.0062}_{-0.0059}$	$0.0586^{+0.0062}_{-0.006}$
ΔN_{tot}	—	< 0.37	< 0.47	$0.06^{+0.23}_{-0.22}$
f_{fs}	—	—	—	$0.381^{+0.022}_{-0.025}$
$N_{\text{fld}}/N_{\text{tot}}$	—	—	< 0.13	< 0.18
H_0 [km/s/Mpc]	$67.26^{+0.48}_{-0.46}$	$68.13^{+1.0}_{-0.76}$	$68.6^{+1.4}_{-1.0}$	$67.9^{+1.7}_{-1.6}$
r_d [Mpc]	$147.43^{+0.24}_{-0.24}$	$146.2^{+0.8}_{-1.3}$	$145.7^{+1.2}_{-1.6}$	$146.8^{+2.2}_{-2.2}$
Ω_m	$0.3149^{+0.0064}_{-0.0064}$	$0.3108^{+0.0071}_{-0.007}$	$0.3079^{+0.0078}_{-0.0083}$	$0.311^{+0.0094}_{-0.0092}$
σ_8	$0.8107^{+0.0051}_{-0.0052}$	$0.816^{+0.0071}_{-0.0063}$	$0.8136^{+0.0057}_{-0.0055}$	$0.8067^{+0.0096}_{-0.01}$

Table 3. Constraints on the extensions to Λ CDM considered in this work using the *Planck* PR4 TT, TE, EE, and lensing likelihoods. Results are presented as in Table 2.

- [11] N.F. Bell, E. Pierpaoli and K. Sigurdson, *Cosmological signatures of interacting neutrinos*, *Phys. Rev. D* **73** (2006) 063523 [[astro-ph/0511410](#)].
- [12] A. Friedland, K.M. Zurek and S. Bashinsky, *Constraining Models of Neutrino Mass and Neutrino Interactions with the Planck Satellite*, **0704.3271**.
- [13] F.-Y. Cyr-Racine and K. Sigurdson, *Limits on Neutrino-Neutrino Scattering in the Early Universe*, *Phys. Rev. D* **90** (2014) 123533 [[1306.1536](#)].
- [14] I.M. Oldengott, C. Rampf and Y.Y.Y. Wong, *Boltzmann hierarchy for interacting neutrinos I: formalism*, *JCAP* **04** (2015) 016 [[1409.1577](#)].
- [15] C.D. Kreisch, F.-Y. Cyr-Racine and O. Doré, *Neutrino puzzle: Anomalies, interactions, and cosmological tensions*, *Phys. Rev. D* **101** (2020) 123505 [[1902.00534](#)].
- [16] R.J. Wilkinson, C. Boehm and J. Lesgourgues, *Constraining Dark Matter-Neutrino Interactions using the CMB and Large-Scale Structure*, *JCAP* **05** (2014) 011 [[1401.7597](#)].
- [17] M.A. Buen-Abad, M. Schmaltz, J. Lesgourgues and T. Brinckmann, *Interacting Dark Sector and Precision Cosmology*, *JCAP* **01** (2018) 008 [[1708.09406](#)].
- [18] M. Archidiacono and S. Hannestad, *Updated constraints on non-standard neutrino interactions from Planck*, *JCAP* **07** (2014) 046 [[1311.3873](#)].
- [19] M. Archidiacono, S. Gariazzo, C. Giunti, S. Hannestad, R. Hansen, M. Laveder et al., *Pseudoscalar—sterile neutrino interactions: reconciling the cosmos with neutrino oscillations*, *JCAP* **08** (2016) 067 [[1606.07673](#)].

	Λ CDM	ΔN_{fs}	ΔN_{fld}	$N_{\text{tot}}, f_{\text{fs}}$
$100\theta_s$	$1.04173^{+0.00024}_{-0.00024}$	$1.04146^{+0.0003}_{-0.00033}$	$1.04189^{+0.00028}_{-0.00027}$	$1.04235^{+0.00061}_{-0.00057}$
ω_b	$0.02217^{+0.00014}_{-0.00014}$	$0.02226^{+0.00015}_{-0.00015}$	$0.02231^{+0.00018}_{-0.00016}$	$0.02222^{+0.00021}_{-0.0002}$
ω_c	$0.1198^{+0.0011}_{-0.0011}$	$0.1216^{+0.002}_{-0.0016}$	$0.1218^{+0.0022}_{-0.0017}$	$0.1199^{+0.0032}_{-0.0032}$
$\ln(10^{10}A_s)$	$3.05^{+0.011}_{-0.011}$	$3.056^{+0.012}_{-0.012}$	$3.05^{+0.011}_{-0.011}$	$3.041^{+0.015}_{-0.015}$
n_s	$0.9631^{+0.004}_{-0.004}$	$0.9673^{+0.0056}_{-0.005}$	$0.9649^{+0.0043}_{-0.0042}$	$0.9587^{+0.0079}_{-0.0077}$
τ_{reio}	$0.0584^{+0.0061}_{-0.0059}$	$0.059^{+0.0061}_{-0.0059}$	$0.0597^{+0.0063}_{-0.006}$	$0.0593^{+0.0062}_{-0.006}$
ΔN_{tot}	—	< 0.34	< 0.37	$0.00^{+0.21}_{-0.21}$
f_{fs}	—	—	—	$0.383^{+0.02}_{-0.022}$
$N_{\text{fld}}/N_{\text{tot}}$	—	—	< 0.11	< 0.15
H_0 [km/s/Mpc]	$67.18^{+0.49}_{-0.48}$	$67.98^{+0.96}_{-0.73}$	$68.2^{+1.2}_{-0.8}$	$67.4^{+1.6}_{-1.5}$
r_d [Mpc]	$147.38^{+0.24}_{-0.25}$	$146.3^{+0.8}_{-1.2}$	$146.1^{+0.9}_{-1.4}$	$147.3^{+2.1}_{-2.0}$
Ω_m	$0.316^{+0.0067}_{-0.0067}$	$0.3123^{+0.007}_{-0.0072}$	$0.3108^{+0.0074}_{-0.0077}$	$0.3146^{+0.0092}_{-0.0091}$
σ_8	$0.8128^{+0.0046}_{-0.0045}$	$0.8177^{+0.0066}_{-0.0057}$	$0.8156^{+0.0052}_{-0.005}$	$0.8086^{+0.0093}_{-0.0094}$

Table 4. Constraints on the extensions to Λ CDM considered in this work using the *Planck* PR4 TT, TE, and EE likelihoods along with the *Planck* PR4 and ACT DR6 lensing likelihoods. Results are presented as in Table 2.

- [20] S. Bashinsky and U. Seljak, *Neutrino perturbations in CMB anisotropy and matter clustering*, *Phys. Rev. D* **69** (2004) 083002 [[astro-ph/0310198](#)].
- [21] D. Baumann, D. Green, J. Meyers and B. Wallisch, *Phases of New Physics in the CMB*, *JCAP* **01** (2016) 007 [[1508.06342](#)].
- [22] K.S. Jeong and F. Takahashi, *Self-interacting Dark Radiation*, *Phys. Lett. B* **725** (2013) 134 [[1305.6521](#)].
- [23] C. Brust, Y. Cui and K. Sigurdson, *Cosmological Constraints on Interacting Light Particles*, *JCAP* **08** (2017) 020 [[1703.10732](#)].
- [24] G. Choi, C.-T. Chiang and M. LoVerde, *Probing Decoupling in Dark Sectors with the Cosmic Microwave Background*, *JCAP* **06** (2018) 044 [[1804.10180](#)].
- [25] T. Brinckmann, J.H. Chang and M. LoVerde, *Self-interacting neutrinos, the Hubble parameter tension, and the cosmic microwave background*, *Phys. Rev. D* **104** (2021) 063523 [[2012.11830](#)].
- [26] N. Blinov and G. Marques-Tavares, *Interacting radiation after Planck and its implications for the Hubble Tension*, *JCAP* **09** (2020) 029 [[2003.08387](#)].
- [27] T. Brinckmann, J.H. Chang, P. Du and M. LoVerde, *Confronting interacting dark radiation scenarios with cosmological data*, *Phys. Rev. D* **107** (2023) 123517 [[2212.13264](#)].
- [28] P. Taule, M. Escudero and M. Garny, *Global view of neutrino interactions in cosmology: The free streaming window as seen by Planck*, *Phys. Rev. D* **106** (2022) 063539 [[2207.04062](#)].

	Λ CDM	ΔN_{fs}	ΔN_{fld}	$N_{\text{tot}}, f_{\text{fs}}$
$100\theta_s$	$1.04188^{+0.00023}_{-0.00023}$	$1.04141^{+0.00036}_{-0.0004}$	$1.04213^{+0.00028}_{-0.00027}$	$1.04247^{+0.00071}_{-0.00067}$
ω_b	$0.02228^{+0.00013}_{-0.00013}$	$0.02239^{+0.00015}_{-0.00015}$	$0.02249^{+0.00018}_{-0.00017}$	$0.02247^{+0.00018}_{-0.00018}$
ω_c	$0.1182^{+0.00081}_{-0.00081}$	$0.1215^{+0.0026}_{-0.0022}$	$0.1232^{+0.0028}_{-0.0028}$	$0.1224^{+0.0033}_{-0.0035}$
$\ln(10^{10}A_s)$	$3.052^{+0.012}_{-0.012}$	$3.059^{+0.013}_{-0.013}$	$3.045^{+0.013}_{-0.013}$	$3.04^{+0.017}_{-0.017}$
n_s	$0.9664^{+0.0036}_{-0.0036}$	$0.9722^{+0.0057}_{-0.0052}$	$0.9675^{+0.0038}_{-0.0038}$	$0.9643^{+0.0072}_{-0.0072}$
τ_{reio}	$0.0615^{+0.006}_{-0.006}$	$0.0611^{+0.006}_{-0.0058}$	$0.0613^{+0.0062}_{-0.0059}$	$0.0614^{+0.0061}_{-0.006}$
ΔN_{tot}	—	< 0.48	< 0.56	$0.23^{+0.20}_{-0.20}$
f_{fs}	—	—	—	$0.381^{+0.025}_{-0.027}$
$N_{\text{fld}}/N_{\text{tot}}$	—	—	< 0.15	< 0.21
H_0 [km/s/Mpc]	$67.9^{+0.37}_{-0.37}$	$69.1^{+1.1}_{-0.8}$	$69.8^{+1.2}_{-1.1}$	$69.5^{+1.3}_{-1.3}$
r_d [Mpc]	$147.69^{+0.21}_{-0.21}$	$145.7^{+1.3}_{-1.6}$	$144.8^{+1.6}_{-1.6}$	$145.2^{+2.0}_{-1.9}$
Ω_m	$0.3061^{+0.0049}_{-0.0049}$	$0.3025^{+0.0054}_{-0.0055}$	$0.3^{+0.0057}_{-0.0057}$	$0.3009^{+0.006}_{-0.006}$
σ_8	$0.8088^{+0.0052}_{-0.005}$	$0.8173^{+0.0083}_{-0.0074}$	$0.814^{+0.0061}_{-0.0059}$	$0.8101^{+0.0096}_{-0.0097}$

Table 5. Constraints on the extensions to Λ CDM considered in this work using the *Planck* PR4 TT, TE, EE, and lensing likelihoods as well as the DESI BAO data. Results are presented as in Table 2.

- [29] A. Das and S. Ghosh, *The magnificent ACT of flavor-specific neutrino self-interaction*, *JCAP* **09** (2023) 042 [[2303.08843](#)].
- [30] SIMONS OBSERVATORY collaboration, *The Simons Observatory: Science goals and forecasts*, *JCAP* **02** (2019) 056 [[1808.07445](#)].
- [31] CMB-S4 collaboration, *CMB-S4 Science Book, First Edition*, [1610.02743](#).
- [32] M. Tristram et al., *Cosmological parameters derived from the final Planck data release (PR4)*, *Astron. Astrophys.* **682** (2024) A37 [[2309.10034](#)].
- [33] J. Carron, M. Mirmelstein and A. Lewis, *CMB lensing from Planck PR4 maps*, *JCAP* **09** (2022) 039 [[2206.07773](#)].
- [34] ACT collaboration, *The Atacama Cosmology Telescope: A Measurement of the DR6 CMB Lensing Power Spectrum and Its Implications for Structure Growth*, *Astrophys. J.* **962** (2024) 112 [[2304.05202](#)].
- [35] ACT collaboration, *The Atacama Cosmology Telescope: DR6 Gravitational Lensing Map and Cosmological Parameters*, *Astrophys. J.* **962** (2024) 113 [[2304.05203](#)].
- [36] DESI collaboration, *DESI 2024 IV: Baryon Acoustic Oscillations from the Lyman Alpha Forest*, [2404.03001](#).
- [37] DESI collaboration, *DESI 2024 VI: Cosmological Constraints from the Measurements of Baryon Acoustic Oscillations*, [2404.03002](#).
- [38] DESI collaboration, *DESI 2024 III: Baryon Acoustic Oscillations from Galaxies and Quasars*, [2404.03000](#).

- [39] S. Raghunathan and Y. Omori, *A Cross-internal Linear Combination Approach to Probe the Secondary CMB Anisotropies: Kinematic Sunyaev–Zel’dovich Effect and CMB Lensing*, *Astrophys. J.* **954** (2023) 83 [2304.09166].
- [40] Z. Hou, R. Keisler, L. Knox, M. Millea and C. Reichardt, *How Massless Neutrinos Affect the Cosmic Microwave Background Damping Tail*, *Phys. Rev. D* **87** (2013) 083008 [1104.2333].
- [41] W. Hu and N. Sugiyama, *Small scale cosmological perturbations: An Analytic approach*, *Astrophys. J.* **471** (1996) 542 [astro-ph/9510117].
- [42] D. Blas, J. Lesgourgues and T. Tram, *The Cosmic Linear Anisotropy Solving System (CLASS) II: Approximation schemes*, *JCAP* **07** (2011) 034 [1104.2933].
- [43] J. Lesgourgues, *The Cosmic Linear Anisotropy Solving System (CLASS) I: Overview*, 1104.2932.
- [44] J. Lesgourgues and T. Tram, *The Cosmic Linear Anisotropy Solving System (CLASS) IV: efficient implementation of non-cold relics*, *JCAP* **09** (2011) 032 [1104.2935].
- [45] W. Hu, *Structure formation with generalized dark matter*, *Astrophys. J.* **506** (1998) 485 [astro-ph/9801234].
- [46] D.J. Fixsen, E.S. Cheng, J.M. Gales, J.C. Mather, R.A. Shafer and E.L. Wright, *The Cosmic Microwave Background spectrum from the full COBE FIRAS data set*, *Astrophys. J.* **473** (1996) 576 [astro-ph/9605054].
- [47] D.J. Fixsen, *The Temperature of the Cosmic Microwave Background*, *Astrophys. J.* **707** (2009) 916 [0911.1955].
- [48] F. Ge, F.-Y. Cyr-Racine and L. Knox, *Scaling transformations and the origins of light relics constraints from cosmic microwave background observations*, *Phys. Rev. D* **107** (2023) 023517 [2210.16335].
- [49] L. Knox and M. Millea, *Hubble constant hunter’s guide*, *Phys. Rev. D* **101** (2020) 043533 [1908.03663].
- [50] M. Zaldarriaga and D.D. Harari, *Analytic approach to the polarization of the cosmic microwave background in flat and open universes*, *Phys. Rev. D* **52** (1995) 3276 [astro-ph/9504085].
- [51] M. Baryakhtar, O. Simon and Z.J. Weiner, *Cosmology with varying fundamental constants from hyperlight, coupled scalars*, *Phys. Rev. D* **110** (2024) 083505 [2405.10358].
- [52] W.T. Hu, *Wandering in the Background: A CMB Explorer*, other thesis, 8, 1995, [astro-ph/9508126].
- [53] J. Froustey, C. Pitrou and M.C. Volpe, *Neutrino decoupling including flavour oscillations and primordial nucleosynthesis*, *JCAP* **12** (2020) 015 [2008.01074].
- [54] S. Gariazzo, P. F. de Salas, O. Pisanti and R. Consiglio, *PARthENoPE revolutions*, *Comput. Phys. Commun.* **271** (2022) 108205 [2103.05027].
- [55] L. Lancaster, F.-Y. Cyr-Racine, L. Knox and Z. Pan, *A tale of two modes: Neutrino free-streaming in the early universe*, *JCAP* **07** (2017) 033 [1704.06657].
- [56] C.D. Kreisch et al., *Atacama Cosmology Telescope: The persistence of neutrino self-interaction in cosmological measurements*, *Phys. Rev. D* **109** (2024) 043501 [2207.03164].
- [57] E. Rosenberg, S. Gratton and G. Efstathiou, *CMB power spectra and cosmological parameters from Planck PR4 with CamSpec*, *Mon. Not. Roy. Astron. Soc.* **517** (2022) 4620 [2205.10869].
- [58] Z. Pan, L. Knox, B. Mulroe and A. Narimani, *Cosmic Microwave Background Acoustic Peak Locations*, *Mon. Not. Roy. Astron. Soc.* **459** (2016) 2513 [1603.03091].

- [59] M. Park, C.D. Kreisch, J. Dunkley, B. Hadzhiyska and F.-Y. Cyr-Racine, Λ CDM or self-interacting neutrinos: How CMB data can tell the two models apart, *Phys. Rev. D* **100** (2019) 063524 [[1904.02625](#)].
- [60] M. Loverde and Z.J. Weiner, Probing neutrino interactions and dark radiation with gravitational waves, *JCAP* **02** (2023) 064 [[2208.11714](#)].
- [61] C.-P. Ma and E. Bertschinger, Cosmological perturbation theory in the synchronous and conformal Newtonian gauges, *Astrophys. J.* **455** (1995) 7 [[astro-ph/9506072](#)].
- [62] A. He, R. An, M.M. Ivanov and V. Gluscevic, Self-interacting neutrinos in light of large-scale structure data, *Phys. Rev. D* **109** (2024) 103527 [[2309.03956](#)].
- [63] D. Camarena, F.-Y. Cyr-Racine and J. Houghteling, Confronting self-interacting neutrinos with the full shape of the galaxy power spectrum, *Phys. Rev. D* **108** (2023) 103535 [[2309.03941](#)].
- [64] J. Torrado and A. Lewis, Cobaya: Code for Bayesian Analysis of hierarchical physical models, *JCAP* **05** (2021) 057 [[2005.05290](#)].
- [65] J. Torrado and A. Lewis, “Cobaya: Bayesian analysis in cosmology.” Astrophysics Source Code Library, record ascl:1910.019, Oct., 2019.
- [66] PLANCK collaboration, Planck 2018 results. V. CMB power spectra and likelihoods, *Astron. Astrophys.* **641** (2020) A5 [[1907.12875](#)].
- [67] A.J. Ross, L. Samushia, C. Howlett, W.J. Percival, A. Burden and M. Manera, The clustering of the SDSS DR7 main Galaxy sample – I. A 4 per cent distance measure at $z = 0.15$, *Mon. Not. Roy. Astron. Soc.* **449** (2015) 835 [[1409.3242](#)].
- [68] BOSS collaboration, The clustering of galaxies in the completed SDSS-III Baryon Oscillation Spectroscopic Survey: cosmological analysis of the DR12 galaxy sample, *Mon. Not. Roy. Astron. Soc.* **470** (2017) 2617 [[1607.03155](#)].
- [69] EBOSS collaboration, The Completed SDSS-IV extended Baryon Oscillation Spectroscopic Survey: measurement of the BAO and growth rate of structure of the luminous red galaxy sample from the anisotropic correlation function between redshifts 0.6 and 1, *Mon. Not. Roy. Astron. Soc.* **500** (2020) 736 [[2007.08993](#)].
- [70] EBOSS collaboration, The Completed SDSS-IV extended Baryon Oscillation Spectroscopic Survey: measurement of the BAO and growth rate of structure of the luminous red galaxy sample from the anisotropic power spectrum between redshifts 0.6 and 1.0, *Mon. Not. Roy. Astron. Soc.* **498** (2020) 2492 [[2007.08994](#)].
- [71] EBOSS collaboration, Completed SDSS-IV extended Baryon Oscillation Spectroscopic Survey: Cosmological implications from two decades of spectroscopic surveys at the Apache Point Observatory, *Phys. Rev. D* **103** (2021) 083533 [[2007.08991](#)].
- [72] A. Lewis, Efficient sampling of fast and slow cosmological parameters, *Phys. Rev. D* **87** (2013) 103529 [[1304.4473](#)].
- [73] W. Hu and M.J. White, A CMB polarization primer, *New Astron.* **2** (1997) 323 [[astro-ph/9706147](#)].
- [74] S. Weinberg, *Cosmology* (2008).
- [75] M. Loverde and Z.J. Weiner, Massive neutrinos and cosmic composition, [2410.00090](#).
- [76] D.J. Eisenstein and W. Hu, Baryonic features in the matter transfer function, *Astrophys. J.* **496** (1998) 605 [[astro-ph/9709112](#)].
- [77] I.J. Allali, A. Notari and F. Rompineve, Dark Radiation with Baryon Acoustic Oscillations from DESI 2024 and the H_0 tension, [2404.15220](#).

- [78] A.G. Riess et al., *A Comprehensive Measurement of the Local Value of the Hubble Constant with 1 km/s/Mpc Uncertainty from the Hubble Space Telescope and the SH0ES Team*, *Astrophys. J. Lett.* **934** (2022) L7 [2112.04510].
- [79] B. Audren, J. Lesgourgues, K. Benabed and S. Prunet, *Conservative Constraints on Early Cosmology: an illustration of the Monte Python cosmological parameter inference code*, *JCAP* **1302** (2013) 001 [1210.7183].
- [80] T. Brinckmann and J. Lesgourgues, *MontePython 3: boosted MCMC sampler and other features*, *Phys. Dark Univ.* **24** (2019) 100260 [1804.07261].
- [81] D. Green, J. Meyers and A. van Engelen, *CMB Delensing Beyond the B Modes*, *JCAP* **12** (2017) 005 [1609.08143].
- [82] A. Mead, C. Heymans, L. Lombriser, J. Peacock, O. Steele and H. Winther, *Accurate halo-model matter power spectra with dark energy, massive neutrinos and modified gravitational forces*, *Mon. Not. Roy. Astron. Soc.* **459** (2016) 1468 [1602.02154].
- [83] A. Chudaykin, M.M. Ivanov, O.H.E. Philcox and M. Simonović, *Nonlinear perturbation theory extension of the Boltzmann code CLASS*, *Phys. Rev. D* **102** (2020) 063533 [2004.10607].
- [84] D. Baumann, D. Green and B. Wallisch, *Searching for light relics with large-scale structure*, *JCAP* **08** (2018) 029 [1712.08067].
- [85] DESI collaboration, “DESI 2024 VII: Cosmological Constraints from the Full-Shape Modeling of Clustering Measurements.” 11, 2024.
- [86] C. Giovanetti, M. Lisanti, H. Liu and J.T. Ruderman, *Joint Cosmic Microwave Background and Big Bang Nucleosynthesis Constraints on Light Dark Sectors with Dark Radiation*, *Phys. Rev. Lett.* **129** (2022) 021302 [2109.03246].
- [87] C. Giovanetti, M. Lisanti, H. Liu, S. Mishra-Sharma and J.T. Ruderman, “LINX: A Fast, Differentiable, and Extensible Big Bang Nucleosynthesis Package.” 8, 2024.
- [88] C. Giovanetti, M. Lisanti, H. Liu, S. Mishra-Sharma and J.T. Ruderman, “Cosmological Parameter Estimation with a Joint-Likelihood Analysis of the Cosmic Microwave Background and Big Bang Nucleosynthesis.” 8, 2024.
- [89] A.C. Sobotka, A.L. Erickcek and T.L. Smith, *Was entropy conserved between BBN and recombination?*, *Phys. Rev. D* **107** (2023) 023525 [2207.14308].
- [90] D. Aloni, M. Joseph, M. Schmaltz and N. Weiner, *Dark Radiation from Neutrino Mixing after Big Bang Nucleosynthesis*, *Phys. Rev. Lett.* **131** (2023) 221001 [2301.10792].
- [91] A.C. Sobotka, A.L. Erickcek and T.L. Smith, *Comprehensive constraints on dark radiation injection after BBN*, *Phys. Rev. D* **109** (2024) 063538 [2312.13235].
- [92] ACT collaboration, *The Atacama Cosmology Telescope: DR4 Maps and Cosmological Parameters*, *JCAP* **12** (2020) 047 [2007.07288].
- [93] SPTPOL collaboration, *Measurements of the Temperature and E-mode Polarization of the Cosmic Microwave Background from the Full 500-square-degree SPTpol Dataset*, **2501.06890**.
- [94] WMAP collaboration, *Nine-Year Wilkinson Microwave Anisotropy Probe (WMAP) Observations: Final Maps and Results*, *Astrophys. J. Suppl.* **208** (2013) 20 [1212.5225].
- [95] WMAP collaboration, *Nine-Year Wilkinson Microwave Anisotropy Probe (WMAP) Observations: Cosmological Parameter Results*, *Astrophys. J. Suppl.* **208** (2013) 19 [1212.5226].
- [96] <https://hyak.uw.edu/>, 2023.
- [97] D. Foreman-Mackey, *corner.py: Scatterplot matrices in python*, *The Journal of Open Source Software* **1** (2016) 24.

- [98] C.R. Harris, K.J. Millman, S.J. van der Walt, R. Gommers, P. Virtanen, D. Cournapeau et al., *Array programming with NumPy*, *Nature* **585** (2020) 357.
- [99] P. Virtanen, R. Gommers, T.E. Oliphant, M. Haberland, T. Reddy, D. Cournapeau et al., *SciPy 1.0: Fundamental Algorithms for Scientific Computing in Python*, *Nature Methods* **17** (2020) 261.
- [100] J.D. Hunter, *Matplotlib: A 2d graphics environment*, *Computing in Science & Engineering* **9** (2007) 90.
- [101] S. Hoyer and J. Hamman, *xarray: N-D labeled arrays and datasets in Python*, *Journal of Open Research Software* **5** (2017) .